

NO-A176 019

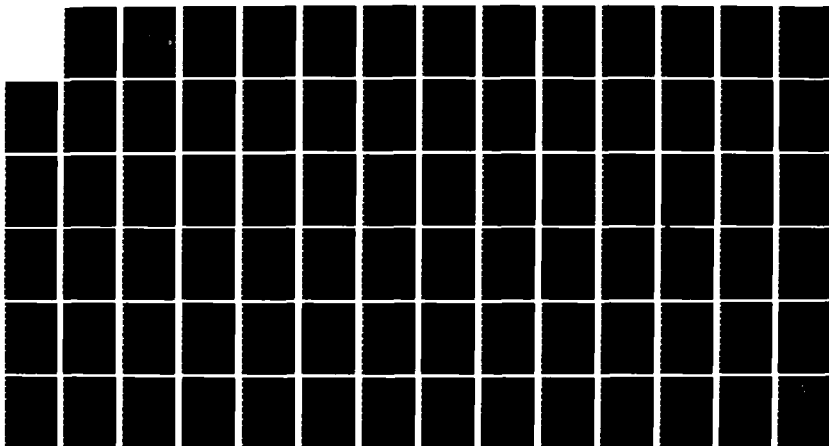
WIND-CURRENT RELATIONSHIPS IN THE OPTIMA DOMAIN OFF THE
NORTHERN CALIFORNIA COAST(U) NAVAL POSTGRADUATE SCHOOL
MONTEREY CA S J SUMMERS SEP 86

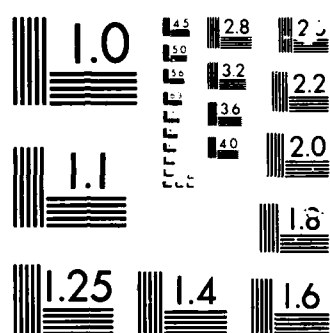
1/1

UNCLASSIFIED

F/G 4/2

NL





AD-A176 019

2

NAVAL POSTGRADUATE SCHOOL

Monterey, California



DTIC
ELECTE
JAN 21 1987
S E D

THESIS

WIND-CURRENT RELATIONSHIPS IN THE
OPTOMA DOMAIN OFF THE NORTHERN
CALIFORNIA COAST

by

Steven J. Summers

September 1986

Thesis Co-Advisors:

Christopher N.K. Mooers
Michele M. Rienecker
Robert L. Smith

Approved for public release; distribution is unlimited

TOP FILE COPY

87 1 21 057

UNCLASSIFIED

SECURITY CLASSIFICATION OF THIS PAGE

AD-A176007

REPORT DOCUMENTATION PAGE

| | | | | |
|---|---|---|--|---------------------------|
| 1a REPORT SECURITY CLASSIFICATION UNCLASSIFIED | | | 1b RESTRICTIVE MARKINGS | |
| 2a SECURITY CLASSIFICATION AUTHORITY | | | 3 DISTRIBUTION/AVAILABILITY OF REPORT Approved for public release; distribution is unlimited | |
| 2b DECLASSIFICATION/DOWNGRADING SCHEDULE | | | | |
| 4 PERFORMING ORGANIZATION REPORT NUMBER(S) | | | 5 MONITORING ORGANIZATION REPORT NUMBER(S) | |
| 6a NAME OF PERFORMING ORGANIZATION Naval Postgraduate School | 6b OFFICE SYMBOL (if applicable) 68 | 7a NAME OF MONITORING ORGANIZATION Naval Postgraduate School | | |
| 6c ADDRESS (City, State, and ZIP Code) Monterey, California 93943-5000 | | 7b ADDRESS (City, State, and ZIP Code) Monterey, California 93943-5000 | | |
| 8a NAME OF FUNDING/SPONSORING ORGANIZATION | 8b OFFICE SYMBOL (if applicable) | 9 PROCUREMENT INSTRUMENT IDENTIFICATION NUMBER | | |
| 8c ADDRESS (City, State, and ZIP Code) | | 10 SOURCE OF FUNDING NUMBERS | | |
| | | PROGRAM ELEMENT NO | PROJECT NO | TASK NO |
| | | WORK UNIT ACCESSION NO | | |
| 11 TITLE (Include Security Classification) WIND-CURRENT RELATIONSHIPS IN THE OPTOMA DOMAIN OFF THE NORTHERN CALIFORNIA COAST | | | | |
| 12 PERSONAL AUTHOR(S) Summers, Steven J. | | | | |
| 13a TYPE OF REPORT Master's Thesis | 13b TIME COVERED FROM TO | 14 DATE OF REPORT (Year, Month, Day) 1986 September | 15 PAGE COUNT 81 | |
| 16 SUPPLEMENTARY NOTATION | | | | |
| 17 COSATI CODES | | | 18 SUBJECT TERMS (Continue on reverse if necessary and identify by block number) | |
| FIELD | GROUP | SUB-GROUP | OPTOMA current meter data | |
| | | | California Current System FNOC wind analyses | |
| | | | ocean mesoscale variability cross-spectrum analysis | |
| 19 ABSTRACT (Continue on reverse if necessary and identify by block number) The oceanic response to time-dependent wind forcing approximately 100-200 km off the Northern California coast is examined through cross-spectrum analysis of current and wind time series. Current meter records 10 months in length from three moorings in deep water 100-200 km off the coast are analyzed in conjunction with surface wind analyses from the Fleet Numerical Oceanography Center (FNOC). Coherence is found between atmospheric and oceanic variables in the "locally forced" band (1-10 day period), in the "planetary wave" band (10-30 day period), and at low frequency (greater than 30 day period), though not in all of these bands for all records. The barotropic and first baroclinic dynamical modes appear to respond to wind forcing at different frequencies for two of the moorings analyzed. There is coherence between alongshore divergence and temperature fluctuations 100 km farther offshore, consistent with offshore advection by current filaments. Evidence of the Sverdrup balance is found for some periods greater than 18 days in the form of coherence between wind stress curl and the current component | | | | |
| 20 DISTRIBUTION/AVAILABILITY OF ABSTRACT <input checked="" type="checkbox"/> UNCLASSIFIED/UNLIMITED <input type="checkbox"/> SAME AS RPT <input type="checkbox"/> DTIC USERS | | | 21 ABSTRACT SECURITY CLASSIFICATION Unclassified | |
| 22a NAME OF RESPONSIBLE INDIVIDUAL Christopher N.K. Mooers | | | 22b TELEPHONE (Include Area Code) 408-646-2552 | 22c OFFICE SYMBOL 68MP |

DD FORM 1473, 84 MAR

83 APR edition may be used until exhausted

All other editions are obsolete

SECURITY CLASSIFICATION OF THIS PAGE

UNCLASSIFIED

UNCLASSIFIED

SECURITY CLASSIFICATION OF THIS PAGE (When Data Entered)

Block 19 - ABSTRACT (CONTINUED)

parallel to the local potential vorticity gradient. Complex bottom topography and the influence of coastal processes in the vicinity of the current meter moorings appear to greatly complicate the flow. There appears to be significant mesoscale variability in the region at scales too small to be resolved by the 100 km spacing of the OPTOMA moorings.

| | |
|--------------------|--|
| Accession For | |
| NTIS GRA&I | <input checked="checked" type="checkbox"/> |
| DTIC TAB | <input type="checkbox"/> |
| Unannounced | <input type="checkbox"/> |
| Justification | |
| By | |
| Distribution/ | |
| Availability Codes | |
| Dist | Avail and/or Special |
| A-1 | |

4
INSPECT

S N 0102- LF-014-6601

UNCLASSIFIED

Approved for public release; distribution is unlimited.

**Wind-Current Relationships in the OPTOMA Domain
Off the Northern California Coast**

by

Steven J. Summers
Lieutenant Commander, United States Navy
B.S., University of Michigan, 1975

Submitted in partial fulfillment of the
requirements for the degree of

MASTER OF SCIENCE IN METEOROLOGY AND OCEANOGRAPHY

from the

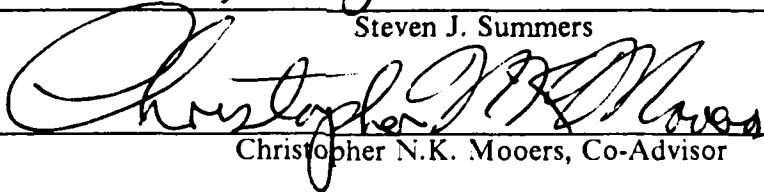
**NAVAL POSTGRADUATE SCHOOL
September 1986**

Author:



Steven J. Summers

Approved by:



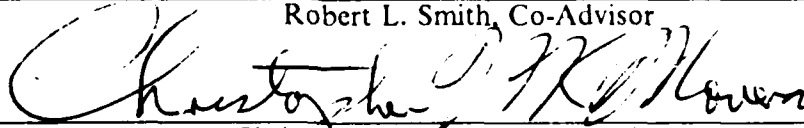
Christopher N.K. Mooers, Co-Advisor



Michele M. Rienecker, Co-Advisor



Robert L. Smith, Co-Advisor



Christopher N.K. Mooers, Chairman,
Department of Oceanography



John N. Dyer,
Dean of Science and Engineering

ABSTRACT

The oceanic response to time-dependent wind forcing approximately 100-200 km off the Northern California coast is examined through cross-spectrum analysis of current and wind time series. Current meter records 10 months in length from three moorings in deep water 100-200 km off the coast are analyzed in conjunction with surface wind analyses from the Fleet Numerical Oceanography Center (FNOC). Coherence is found between atmospheric and oceanic variables in the "locally forced" band (1-10 day period), in the "planetary wave" band (10-30 day period), and at low frequency (greater than 30 day period), though not in all of these bands for all records. The barotropic and first baroclinic dynamical modes appear to respond to wind forcing at different frequencies for two of the moorings analyzed. There is coherence between alongshore divergence and temperature fluctuations 100 km farther offshore, consistent with offshore advection by current filaments. Evidence of the Sverdrup balance is found for some periods greater than 18 days in the form of coherence between wind stress curl and the current component parallel to the local potential vorticity gradient. Complex bottom topography and the influence of coastal processes in the vicinity of the current meter moorings appear to greatly complicate the flow. There appears to be significant mesoscale variability in the region at scales too small to be resolved by the 100 km spacing of the OPTOMA moorings.

TABLE OF CONTENTS

| | | |
|------|--|----|
| I. | INTRODUCTION | 11 |
| A. | BACKGROUND AND OBJECTIVES | 11 |
| B. | THE STUDY AREA | 12 |
| | 1. Oceanography | 12 |
| | 2. Meteorology | 14 |
| II. | THE WIND FORCING | 15 |
| A. | WIND FIELDS | 15 |
| | 1. Seasonal Variability | 15 |
| B. | WIND STRESS | 18 |
| | 1. Seasonal Variability | 18 |
| | 2. Autocorrelation Functions and Time Scales | 18 |
| | 3. Spectrum Analysis | 21 |
| C. | WIND STRESS CURL | 21 |
| III. | THE CURRENTS | 30 |
| A. | CURRENT DATA | 30 |
| | 1. Autocorrelation Functions and Time Scales | 30 |
| | 2. Spectrum Analysis | 33 |
| | 3. Dynamical Mode Decomposition | 39 |
| B. | SPATIAL VARIABILITY OF CURRENTS | 44 |
| | 1. Vertical Coherence | 44 |
| | 2. Horizontal Coherence | 44 |
| IV. | THE CURRENT RESPONSE TO WINDS | 47 |
| A. | WIND STRESS/CURRENT CROSS-SPECTRUM ANALYSIS | 48 |
| B. | CROSS-SPECTRUM ANALYSIS WITH WIND STRESS CURL | 51 |
| | 1. Wind Stress Curl Versus Temperature and its Time Derivative | 51 |

| | |
|---|----|
| 2. Wind Stress Curl and Temperature Versus Current Horizontal Divergence | 52 |
| 3. The Sverdrup Balance | 53 |
| C. WIND STRESS/DYNAMICAL MODE CROSS-SPECTRUM ANALYSIS | 57 |
| 1. Mooring M1 | 57 |
| 2. Mooring M2 | 57 |
| D. DISCUSSION | 57 |
| V. SUMMARY AND CONCLUSIONS | 67 |
| A. SUMMARY | 67 |
| 1. Locally Forced Response (1-10 day period) | 67 |
| 2. Planetary Wave Response (10-30 day periods) | 67 |
| 3. Sverdrup Balance Response (> 30 day periods) | 68 |
| 4. Effects of Bottom Topography | 68 |
| 5. Coastal Effects | 68 |
| B. RECOMMENDATIONS | 69 |
| APPENDIX A: PROCESSING AND ANALYSIS OF FNOC WIND DATA | 70 |
| LIST OF REFERENCES | 77 |
| INITIAL DISTRIBUTION LIST | 79 |

LIST OF TABLES

| | | |
|----|---|----|
| 1. | WIND STRESS STATISTICS | 20 |
| 2. | INTEGRAL TIME SCALES AND DECORRELATION TIMES FOR WIND STRESS FIELDS | 20 |
| 3. | FNOC WIND STRESS CURL MONTHLY MEANS AND LONG TERM MEANS OF NELSON (1977) | 26 |
| 4. | CURRENT METER DEPTHS AND RECORDED VARIABLES USED IN ANALYSIS | 32 |
| 5. | STATISTICS OF CURRENT AND TEMPERATURE RECORDS | 36 |
| 6. | INTEGRAL TIMES SCALES AND DECORRELATION TIMES FROM CURRENT RECORDS | 39 |
| 7. | COHERENT PEAKS BETWEEN WIND STRESS AND CURRENT COMPONENTS | 50 |
| 8. | CURRENT PEAKS BETWEEN WIND STRESS AND CURRENT PARALLEL TO PRINCIPAL AXIS DIRECTION | 51 |

LIST OF FIGURES

| | | |
|------|--|----|
| 2.1 | FNOC grid point and current meter mooring locations. The dashed line outlines the domain of the OPTOMAII survey during summer 1984. | 16 |
| 2.2 | Monthly mean wind with standard deviation ellipses for May 1985 (top) and November 1984 (bottom). | 17 |
| 2.3 | Time series of wind stress at FNOC grid points in the vicinity of OPTOMA moorings. From the top: grid points G, K, H, L. Units dyn/cm ² | 19 |
| 2.4 | Total spectra of wind stress at FNOC grid points G, H, K, L. | 22 |
| 2.5 | Auto-rotary spectrum of the wind stress field at grid point G (typical of all ocean grid points). Thick line: total spectrum, dashed line: anticlockwise, thin line: clockwise. | 23 |
| 2.6 | Spectra of meridional (a) and zonal (b) wind stress components, grid point G. | 24 |
| 2.7 | Comparison of wind stress curl monthly means for nearshore (top) and offshore (bottom) cases. Solid line: present study, dashed line: Nelson (1977). | 27 |
| 2.8 | Wind stress curl spectra for nearshore (a) and offshore (b) cases. | 28 |
| 2.9 | Autospectrum of wind stress curl over the OPTOMA domain for the period covering the current meter moorings. | 29 |
| 3.1 | Locations of moorings M1, M2, M3, and CMMW10 with respect to bathymetry. Depths are in meters. Contour interval is 200 m. | 31 |
| 3.2 | Current time series from mooring M1. Depths from top are 175, 375, and 3250 m. Units: cm/s. | 33 |
| 3.3 | Current time series from mooring M2. Depths from top are 145, 340, 800, 1190, and 3560 m. Units: cm/s. | 34 |
| 3.4 | Current time series from mooring M3. Depths from top are 350, 800, and 1185 m. Units: cm/s. | 35 |
| 3.5 | Monthly mean and standard error of selected current records at M1, M2 and M3. Units: cm/s. | 37 |
| 3.6 | Autocorrelation functions of zonal and meridional components of M1-375, M2-340, and M3-340. | 38 |
| 3.7 | Auto-rotary spectra of current at M2-340, (typical of other records). Thick line: total spectrum, dashed line: anticlockwise, thin line: clockwise. | 40 |
| 3.8 | As in Figure 3.7, but for M1-3250. | 41 |
| 3.9 | As in Figure 3.7, but for M2-3560. | 42 |
| 3.10 | First three baroclinic normal modes computed from CTD casts within 50 km of M1, M2, and M3. | 43 |

| | | |
|------|---|----|
| 3.11 | Coherence between pairs of meridional current components at M2 as a function of vertical separation (Δz). | 45 |
| 3.12 | Coherence between current components parallel to the principal axis direction of M1-375, M2-340, and M3-350. | 46 |
| 4.1 | Mean vectors and standard deviation ellipses for wind stress at FNOC grid points A through P over the period of the study. | 49 |
| 4.2 | Coherence and phase between wind stress curl and horizontal current divergence at 350 m. | 54 |
| 4.3 | Time series of (from the top) horizontal divergence, alongshore divergence, temperature at M3-350, and $\nabla \times \tau$ | 55 |
| 4.4 | Coherence and phase between alongshore divergence (from M1 and M2) and temperature at M3-350. | 56 |
| 4.5 | Coherence and phase between wind stress curl and current component 30° east of north at M1-375. | 58 |
| 4.6 | As in Figure 4.5, but for M2-340 and 120° east of north. | 59 |
| 4.7 | Coherence and phase between meridional wind stress and meridional component of barotropic mode, M1. | 60 |
| 4.8 | As in Figure 4.7, but with the first baroclinic mode, M1. | 61 |
| 4.9 | As in Figure 4.7, but with the barotropic mode, M2. | 62 |
| 4.10 | As in Figure 4.7, but with the first baroclinic mode, M2. | 63 |
| 4.11 | As in Figure 4.7, but with the barotropic mode, CMMW10. | 65 |
| 4.12 | As in Figure 4.7, but with the first baroclinic mode, CMMW10. | 66 |
| A.1 | Time series of wind stress curl derived from square (top) and triangular (bottom) schemes. | 74 |
| A.2 | Autospectra of wind stress curl computed with square (a) and triangular (b) schemes. | 74 |
| A.3 | Coherence and phase between square and triangular schemes. | 75 |

ACKNOWLEDGEMENTS

The guidance and support of my co-advisors, Dr. Christopher N.K. Mooers, Dr. Michele M. Rienecker, and Dr. Robert L. Smith, have been invaluable to me in the preparation of this thesis. Dr. Mooers first stimulated my interest in dynamical oceanography, provided the motivation for this study, and shaped its progress along the way. Special thanks are due Dr. Rienecker, who developed the spectral analysis computer programs used in this study and assisted me in debugging many other programs. She has generously given many hours of her time, and her advice and suggestions on the matters of writing style, interpretation of the results, and many other facets of this project have been invaluable. Dr. Smith shared his results from a separate analysis (with other investigators) at Oregon State University of the current records and provided valuable suggestions and insight into the many aspects of this study. All three co-advisors read several preliminary drafts of this thesis and gave generously of their expertise. The opportunity to work with experts of the highest caliber such as Dr. Mooers, Dr. Rienecker, and Dr. Smith has been a rewarding and enjoyable experience.

Dr. Smith, with his colleagues at Oregon State University, deployed and retrieved the current meter moorings and performed initial post-processing of the data. The data archiving division at FNOC provided the surface wind analyses. Computing resources were provided by the W.R. Church Computer Center.

Finally, my wife Becky has my deepest love and gratitude for her patience and support. She contributed directly to this thesis in ways that may not be readily apparent to the reader, but were essential to its successful completion.

I. INTRODUCTION

A. BACKGROUND AND OBJECTIVES

The Navy has experienced a dramatic increase in the sophistication of its ship and aircraft based weapons systems and sensors over the last decade. Coincident with this increase in equipment capability has been an increased requirement to understand ocean structure and variability and their impact upon naval operations. The data currently used to describe and predict ocean structure are at best sparse, especially in light of the spatial and temporal scales typical of the upper ocean. An understanding of the relationship between atmospheric forcing and ocean currents is an important step toward describing and, ultimately, predicting such ocean variability with sparse oceanic and atmospheric data.

The Ocean Prediction Through Observations, Modeling, and Analysis (OPTOMA) program is a joint Naval Postgraduate School/Harvard University project, sponsored by the Office of Naval Research, with goals of developing techniques for numerical forecasting of mesoscale ocean variability (such as eddies and meandering jets). OPTOMA has concentrated its efforts off the continental slope in an eastern boundary current regime. The present effort is focused upon a "test block" of ocean in the California Current System (CCS). OPTOMA is developing an ocean descriptive-predictive system for four-dimensional data assimilation which could benefit directly from a better understanding of the relationship of ocean currents to atmospheric forcing.

Previous studies have examined the oceanic response to atmospheric forcing in the mid-latitude North Pacific. Halliwell and Allen (1984) examined the response of sea level fluctuations in 1973 along the west coast of North America to alongshore wind stress at large scale (> 1000 km). They found atmospheric forcing to be most effective along northern California and Oregon. Forced fluctuations in sea level propagated poleward away from this forcing area, causing local sea level along the coast to be correlated with alongshore wind stress earlier in time and at a distant equatorward location.

Niiler and Koblinsky (1985) examined long (~ 10 month) moored current meter records from far offshore in the eastern North Pacific with wind analyses from the U.S.

Navy Fleet Numerical Oceanography Center (FNOC) and found wind stress curl to be significantly correlated with deep (below 150 m) ocean currents at periods of 10-100 days. Much closer to the coast, Noble *et.al.* (1986) analyzed current meter records over the northern California slope and adjacent basin and found some weak evidence of wind-forced flow in both areas at periods less than 10 days.

Stabeno and Smith (1986) analyzed current meter data from 11 moorings that were part of the Oregon State University/Sandia National Laboratory Low-Level Waste Ocean Disposal (LLWOD) Program (Heath *et. al.*, 1984) and 3 moorings that are part of the OPTOMA program. They found evidence of lens-like eddies in the currents within 1500 m of the bottom in the LLWOD records (100-200 km seaward of the 4000 m isobath), and much less low frequency (eddy) energy in the near-bottom OPTOMA records (shoreward of the 4000 m isobath). They also found evidence of the influence of CCS cold filaments originating near Point Arena in the near-surface OPTOMA records.

The OPTOMA moorings analyzed by Stabeno and Smith (1986) were deployed in 1984-85 off northern California by Oregon State University in association with the OPTOMA program (Smith *et. al.*, 1986). FNOC surface wind analyses covering the mooring period and area are also available. The objective of this research is a detailed examination of the FNOC surface wind analyses and OPTOMA current meter data and the relationship between them. Specifically, the spectra of the current meter and wind records will be examined with the goal of better understanding how ocean currents respond over depth to wind forcing in the region equatorward of the Mendocino Escarpment. Knowledge of the oceanic response to atmospheric forcing from studies such as this will be useful in assessing and, perhaps, improving the modeling/prediction of wind-driven ocean circulation. The accurate prediction of ocean mesoscale variability (of which the wind-driven circulation is a component) is a vital prerequisite to the accurate forecasting of acoustic energy propagation that is needed by operational Navy antisubmarine warfare forces to efficiently and effectively carry out their missions.

B. THE STUDY AREA

1. Oceanography

The current meter moorings are located within the OPTOMA NOCAL domain, an open ocean region nominally 300 km square. It is just offshore of the

continental slope with a mean water depth of about 4000 m. The NOCAL domain is 100-200 km south of the Mendocino Escarpment and is within 150 km of seamounts.

The long-term climatological mean flow of the CCS is usually considered to be broad (~ 1000 km), shallow (~ 500 m), and slow (~ 4 cm/sec) (Hickey, 1978). The CCS forms the eastern boundary current of the North Pacific gyre and lies just to the east of the climatological North Pacific atmospheric ridge (see below), leading to the predomination of southward to southeastward winds during all but the winter season over the area south of 40N. These winds induce offshore surface Ekman transport and, consequently, coastal upwelling from February or March through August or September off Northern California. Due to a wind maximum ~ 300 km offshore they also produce a positive wind stress curl which induces Ekman suction (i.e., open ocean upwelling) from the coast to the offshore wind maximum. Similarly, there is a negative wind stress curl and open ocean downwelling seaward of the wind maximum.

In contrast to its climatological mean flow, the instantaneous CCS is now known to be a very complex system of meandering jets, mesoscale eddies, and current filaments (Mooers and Robinson, 1984). The CCS coastal circulation structure varies seasonally, with northward flow in the winter, southward flow in the summer, and a northward undercurrent with a southward surface current in the summer and fall (Hickey, 1979). Meander patterns (which appear as large, cold filaments extending offshore) can be seen in satellite infrared images of the west coast of North America. From a series of dynamical model simulations, Ikeda and Emery (1984) concluded that these features stem from interaction of the mean current with bottom topography and grow because of baroclinic instability associated with vertical shear between the surface current and the undercurrents (during summer and fall). They further concluded that, in all seasons, irregularities in bottom topography generate meanders in the CCS with horizontal scales similar to that of the topography. There is also evidence from model results and hydrographic survey data for the existence of barotropic instability processes in the OPTOMA domain (Robinson *et al.*, 1986).

Philander and Yoon (1982) demonstrated, using numerical model experiments with both steady winds and fluctuating winds of various periods, that atmospheric forcing also plays a significant role in the complexity of eastern boundary current regions such as the CCS. Time dependent winds parallel to the coast create a vorticity source in the upper layers of the ocean near the coast which excite Rossby waves. These waves give rise to a complex system of poleward and equatorward currents near

the coast that is superimposed on the mean flow (driven by the large-scale wind stress curl).

Carton (1984) used the results of numerical experiments to show that oceanic response to isolated storms along an eastern boundary depends upon the ratio of storm duration to the time a coastal trapped wave takes to propagate to the point at which the response is measured. Carton found that the model ocean response to a storm was a vertically independent flow in the direction of the wind followed by an undercurrent flowing in the opposite direction. He suggested that variations in alongshore topography neglected in his study may be important sources of energy for vertically-varying waves.

The combined effects of variability in the atmospheric forcing, the instabilities related to coastal effects (such as upwelling), and complex bottom topography make the nature of the ocean in this study area very complicated.

2. Meteorology

The properties of wind fluctuations along the west coast of North America vary over a wide range of time scales (Halliwell and Allen, 1986). Winter winds are primarily driven by propagating cyclones and anticyclones, and hence wind properties can fluctuate over time scales as short as several days. The summer winds are dominated by the effects of two quasi-permanent pressure systems - the North Pacific subtropical high and the southwest U.S. thermal low. Propagating surface cyclones (weaker than those of the winter) interact with the subtropical high to influence summertime winds. The subtropical high often strengthens and shifts toward the coast, causing intervals of strong equatorward (alongshore) winds off the California coast. The high occasionally builds far to the north for days to weeks at a time, preventing propagating cyclones from affecting the California coast.

II. THE WIND FORCING

A. WIND FIELDS

Wind fields were extracted from the FNOC surface wind analyses for 16 grid points off the northern California coast, Figure 2.1, for the 13-month period June 1984 through June 1985. For ease of reference, the grid points are designated A through P. The FNOC surface wind analysis and procedures used to construct the wind, wind stress, and wind stress curl time series used in this study are described in Appendix A.

1. *Seasonal Variability*

Monthly mean wind shows a distinct seasonal variability, Figure 2.2. In summer (represented by May 1985 in Figure 2.2), the mean has an equatorward component at all grid points. Within about 300 km of the coast the mean tends to be aligned with the coastline. The mean becomes more directly southward farther away from the coast. This anticyclonic mean flow pattern is associated with the North Pacific subtropical high (Halliwell and Allen, 1986). In virtually all cases, the mean is significant at the 95% level. The standard deviation ellipses are generally oriented with their major axes alongshore. The major axis direction, θ , is that of minimum Reynold's stress, defined by

$$\tan 2\theta = 2\langle u'v' \rangle / (\langle u'^2 \rangle - \langle v'^2 \rangle),$$

where u' and v' are the perturbations from the time mean of the zonal and meridional wind components (respectively), and the angle brackets denote time-averaging. The standard deviations are generally larger for the more poleward grid points and are also larger close to the coast. The larger standard deviations observed at the poleward grid points reflect the position of the storm track which is poleward of the subtropical high: synoptic-scale atmospheric disturbances propagating through this region account for the larger observed standard deviations.

In winter (represented by November 1984 in Figure 2.2), the mean is smaller and the standard deviations larger than in summer and frequently the means are not statistically significant at the 95% level. The winter storm track for synoptic-scale atmospheric disturbances is southward of its summer counterpart, with many major storms passing through the study area. Synoptic-scale fluctuations in the surface

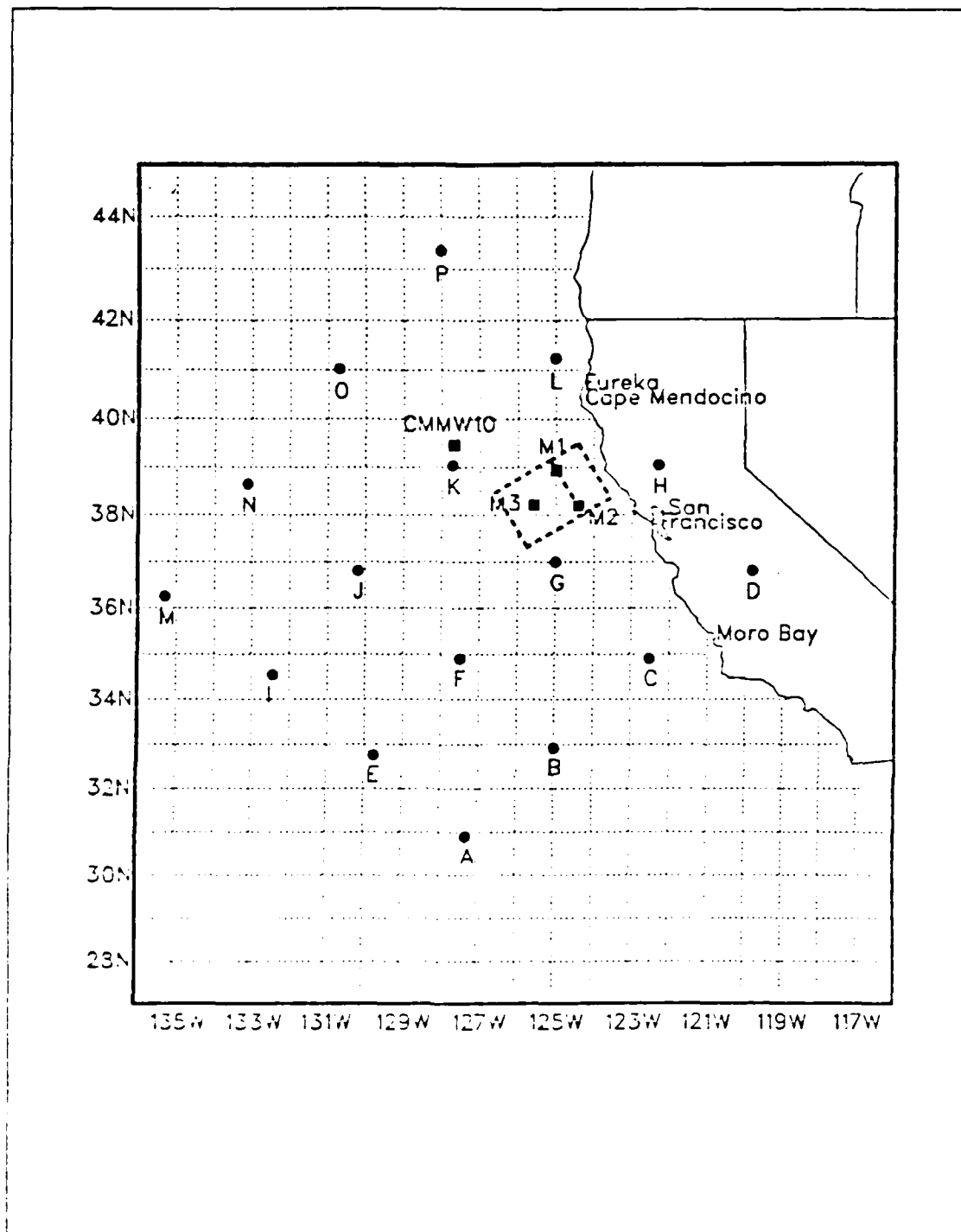


Figure 2.1. FNOG grid point and current meter mooring locations. The dashed line outlines the domain of the OPTOMAT survey during summer 1984.

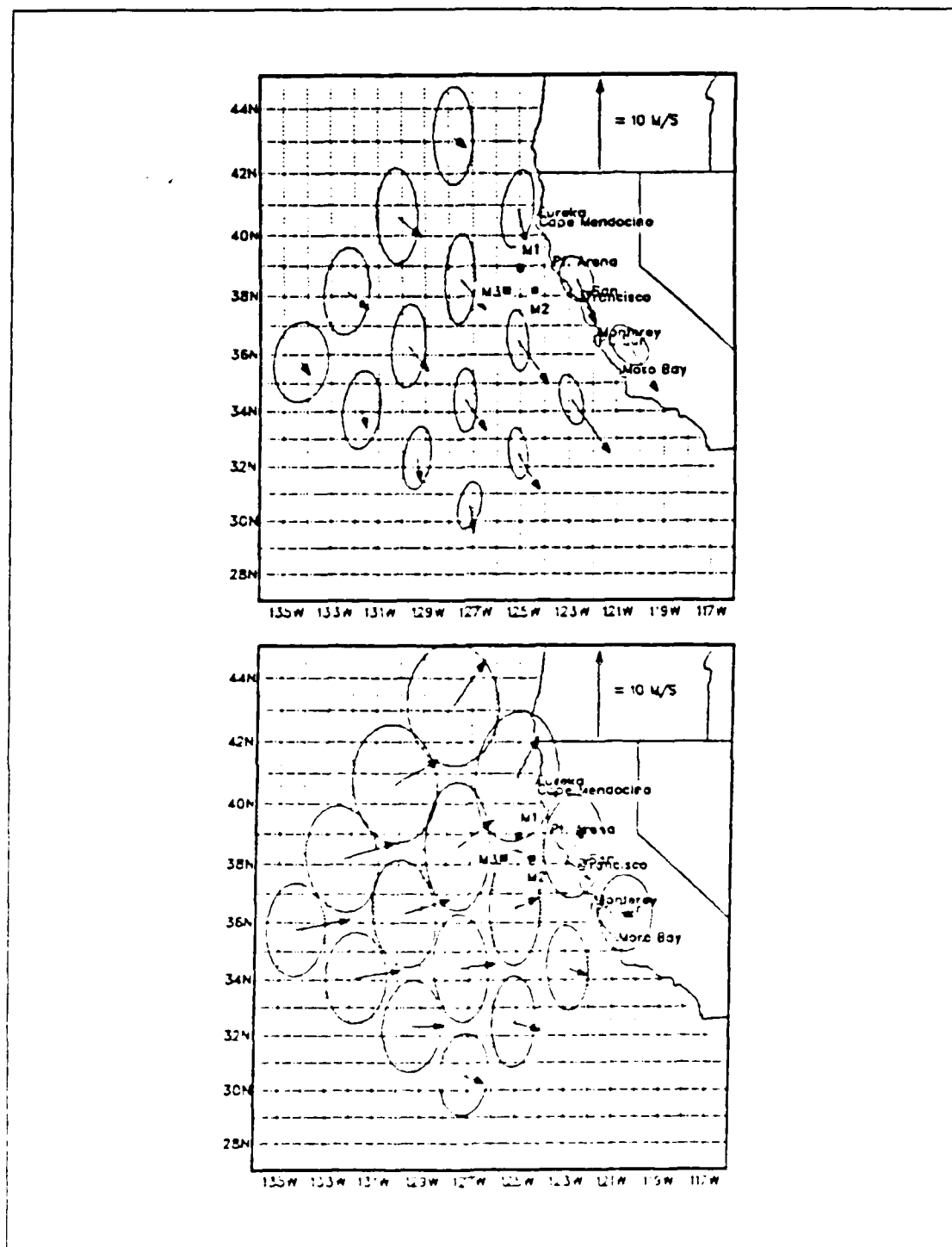


Figure 2.2 Monthly mean wind with standard deviation ellipses for May 1985 (top) and November 1984 (bottom).

atmospheric pressure gradient caused by the propagation of storms through and near the study area alter the magnitude and direction of surface winds. These storms occur every few days in winter, accounting for the larger deviations and many changes in sign in winter wind velocities over periods of a few days, and, consequently, for the smaller mean observed in winter.

B. WIND STRESS

Wind stress is computed using the bulk aerodynamic method with the neutral flux drag coefficient of Large and Pond (1981), Appendix A. Wind stress is a more dynamically relevant variable than is wind and hence, all future references will be to wind stress unless otherwise noted.

1. Seasonal Variability

Largest magnitude events in the wind stress time series generally occur in winter and spring months, Figure 2.3. There are reversals in the sign of meridional component of the wind stress time series from October 1984 through March 1985. The meridional wind stress is equatorward from April through June 1985 with the exception of a few short, small magnitude poleward events, Figure 2.3. The zonal mean is eastward and the meridional mean is equatorward at all points, Table 1. The mean wind stress is different in direction near the coast from the general pattern over water, possibly indicating that the FNOC wind fields are sensitive to coastal topography, although Halliwell and Allen (1986) show that the winds derived from FNOC pressure fields do not *correctly* represent the coastal boundary layer effects.

2. Autocorrelation Functions and Time Scales

The wind stress time series are low-pass filtered using filter weights as suggested by Thompson (1983) with a cutoff frequency of about 1 cpd and half-power point at about 0.6 cpd (e.g., ~ 40 hour period). From complex autocorrelations (calculated for lags up to 68 days, i.e., $N/4$, where N is the record length), the integral correlation time scale of wind stress for grid points G, H, K, and L are typically 1.5 - 2.0 days for the zonal component and 2.5 - 3.0 days for the meridional component, Table 2. Wind stress at the point over land (point H) has an integral time scale of about 3.0 days for both components. Here, integral time scale, τ_i (as suggested by Richman *et. al.*, 1976) is given by

$$\tau_i = \Delta t [1 + 2 \sum_{k=1}^K R_k^2].$$

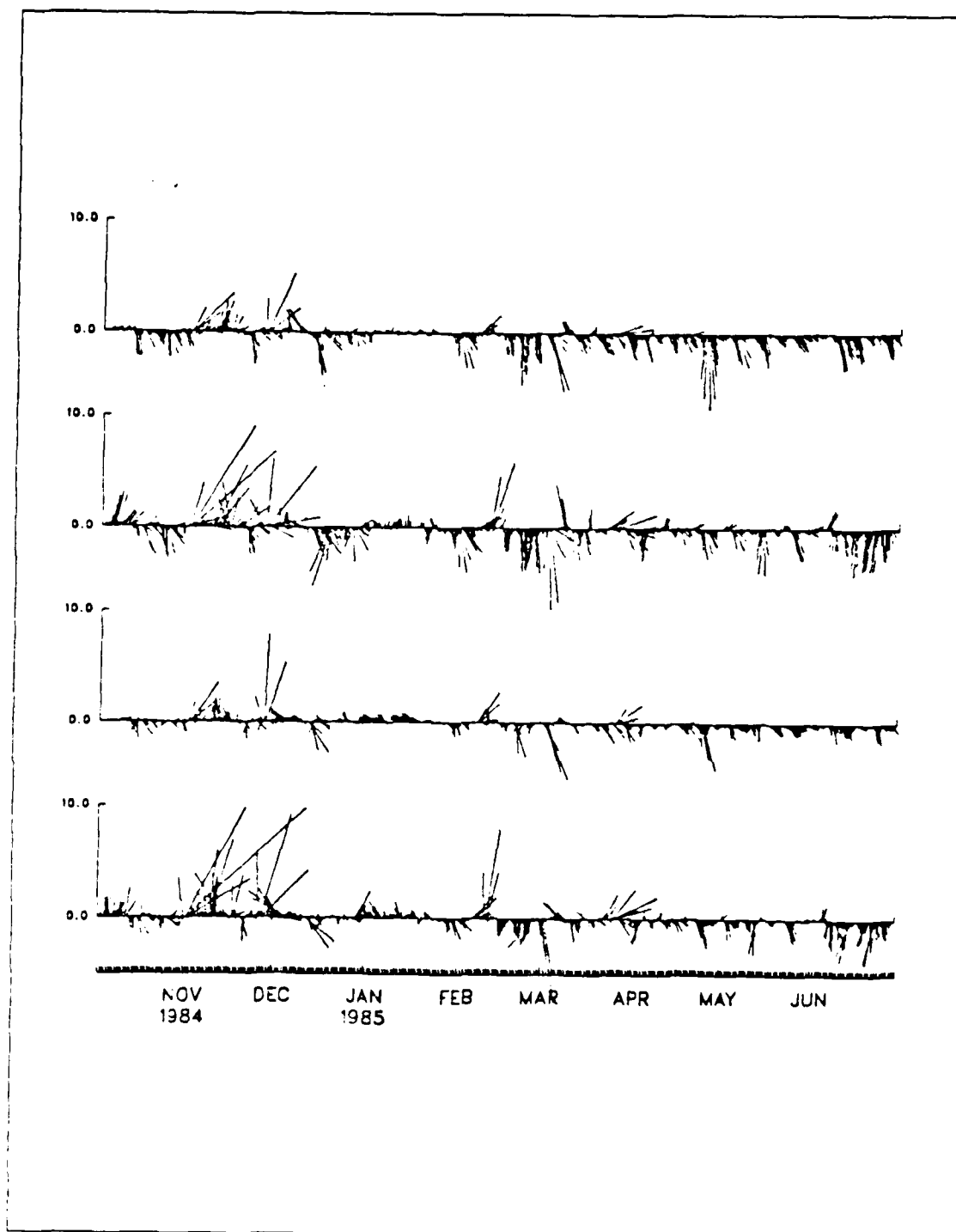


Figure 2.3 Time series of wind stress at FNOG grid points in the vicinity of OPTOMA moorings. From the top: grid points G, K, H, L. Units dyn cm⁻².

TABLE 1
WIND STRESS STATISTICS

| GRID-PT | $\langle u \rangle^*$ | σ_u^* | $\langle v \rangle^*$ | σ_v^* |
|---------|-----------------------|--------------|-----------------------|--------------|
| G | 0.3 | 0.6 | -0.5 | 1.2 |
| H | 0.1 | 0.4 | -0.2 | 0.8 |
| K | 0.3 | 0.8 | -0.3 | 1.6 |
| L | 0.1 | 0.8 | -0.1 | 1.4 |

* units: dyn/cm²

< > denotes mean

σ : standard deviation

TABLE 2
INTEGRAL TIME SCALES AND DECORRELATION TIMES
FOR WIND STRESS FIELDS

| GRID PT | INT. TIME SCALE * | | DECORR. TIME * | |
|---------|-------------------|----------|----------------|----------|
| | τ_x | τ_y | τ_x | τ_y |
| G | 1.9 | 2.9 | 1.2 | 1.8 |
| H | 2.9 | 2.8 | 1.6 | 1.2 |
| K | 1.8 | 2.5 | 1.2 | 1.5 |
| L | 1.4 | 2.5 | 1.1 | 1.3 |

*: units are days

where R_k is the correlation at lag $k\Delta t$ and K is the maximum lag used in the correlation analysis (theoretically, a large lag at which the autocorrelation function has died out). The integral time scale is a measure of the time after which a new independent event may be considered to occur. The decorrelation time, T_d , is the time for which

$$R(T_d) = 1/e.$$

These time scales indicate fluctuations in the wind records with 1-to-2 day time scales, consistent with the period of wintertime synoptic-scale atmospheric disturbances in the study area.

3. *Spectrum Analysis*

Characteristics of the wind stress field in the frequency domain are studied utilizing the rotary spectra techniques described by Gonella (1972) and Mooers (1973). The filtered wind stress time series at FNOC grid points G, H, K, and L are subdivided into five 360-point pieces with 50% overlap. Linear trends are removed from the series, a Hanning window smoother is applied to the spectrum of each piece, and piece averaging is performed to yield spectrum estimates with 10 degrees of freedom.

The wind stress spectra at all four grid points are similar. All four spectra are white for periods greater than about 10 days and red for periods less than 5 days, Figure 2.4. The spectra of wind stress at points K and L have a peak at periods between 5 and 10 days, Figure 2.4. The energy level of the spectrum at point H (over land) is significantly lower at all frequencies than those of the spectra of the other three points, Figure 2.4. In all cases the clockwise (anticyclonic) spectrum is not significantly different from the anticlockwise (cyclonic) at the 90% significance level, Figure 2.5. Equal clockwise and anticlockwise components of the spectrum is an indication of rectilinear vice rotary motion. The spectra of all meridional wind stress components (as represented by point G) are about an order of magnitude more energetic than their zonal counterparts, Figure 2.6.

C. WIND STRESS CURL

Time series of wind stress curl are computed (see Appendix A) for a nearshore and an offshore case over a 12-month period to examine the spatial variability of such time series derived from FNOC wind data. The average wind stress curl ($\nabla \times \tau$) over the area denoted by grid points F, G, J, and K (with nominal center at 37N, 128W) is computed as the offshore case. The nearshore case is computed over the area denoted by points G, K, and L (with nominal center at 39N, 125W). The additional truncation error introduced by using a 3-point finite difference approximation to compute $\nabla \times \tau$ at the nearshore position has negligible impact on the curl spectrum (see discussion, Appendix A). Monthly means of these curl time series were compared to those of Nelson (1977), who computed long term mean wind stress curl values from ship reports for 1° squares over the CCS. These results generally agree with Nelson's (i.e., same

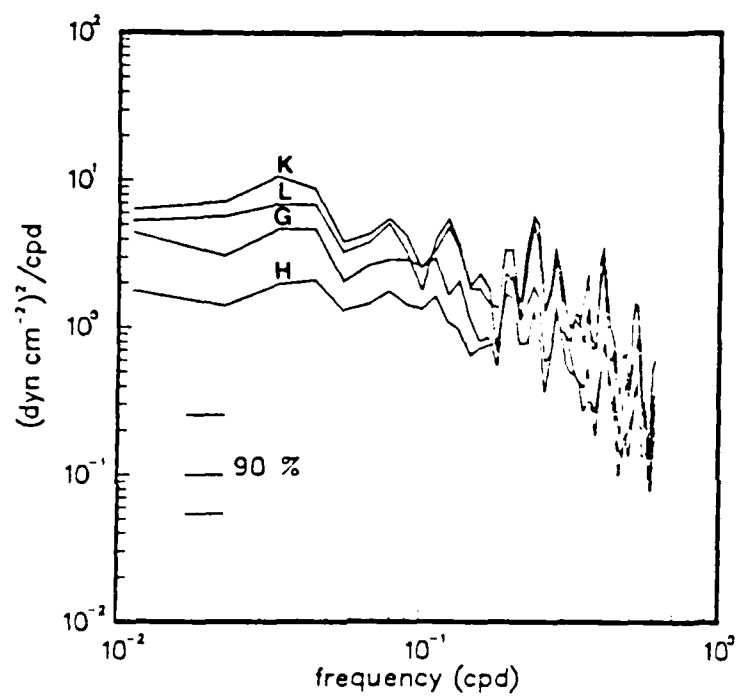


Figure 2.4 Total spectra of wind stress at ENOC grid points G, H, K, L.

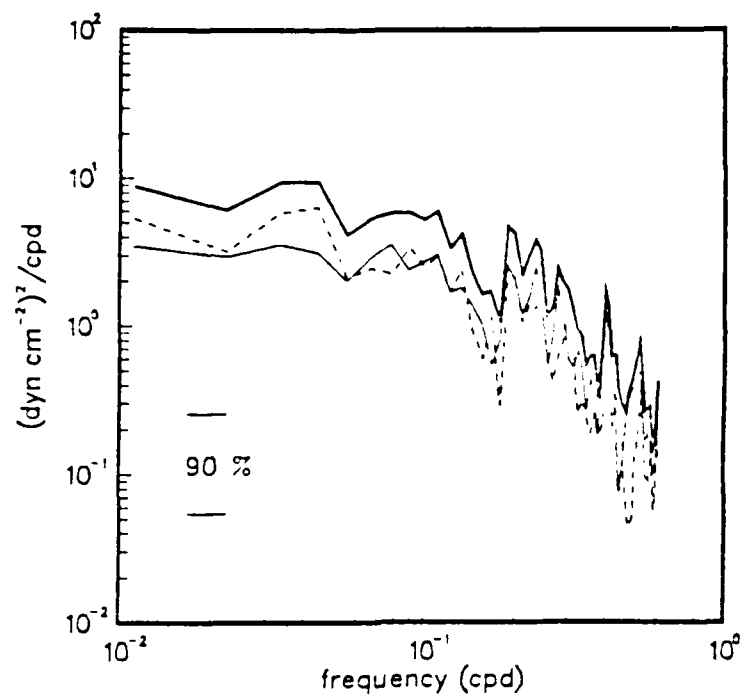


Figure 2.5 Auto-rotary spectrum of the wind stress field at grid point G (typical of all ocean grid points). Thick line: total spectrum, dashed line: anticlockwise, thin line: clockwise.

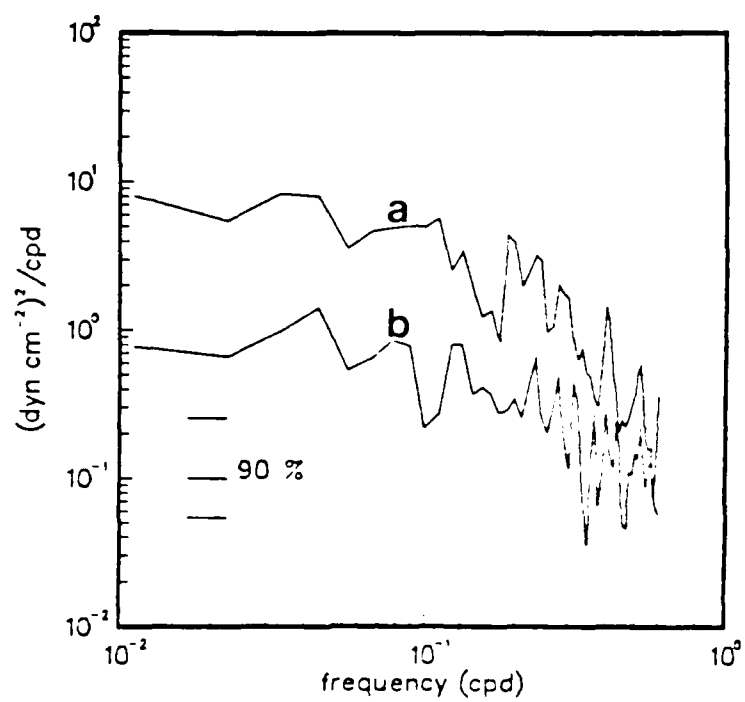


Figure 2.6 Spectra of meridional (a) and zonal (b) wind stress components, grid point G.

sign and order of magnitude in most cases), Table 3, usually positive along the coast and negative offshore. The agreement between the monthly means of this study and those of Nelson's climatology is greater for the offshore case than for the nearshore case, Figure 2.7. The differences noted between the results of this study and Nelson's climatology, however, do not necessarily require that one of them be in error. Possible explanations of the differences are:

- Nelson's climatology gives the long term mean (over a period > 100 years), and the resultant smoothing could decrease the mean values.
- Nelson's climatology is based upon surface observations that are subject to many smaller scale atmospheric phenomena such as variation of the marine atmospheric boundary layer depth. The FNOC winds used in this study reflect synoptic scale atmospheric disturbances and are generally insensitive to the smaller scale processes that affect *in situ* surface observations (Halliwell and Allen, 1986).
- Calculation of wind stress curl on large grids such as the FNOC grid can underestimate the values by as much as 50% (Saunders, 1976).
- 1984-85 is not necessarily a typical year.

In the auto-spectra of the two (offshore and nearshore) wind stress curl time series, there appears to be less energy in the offshore $\nabla \times \tau$ as evidenced by the lower energy in its spectrum at low frequencies (periods < 12 days), and at periods of about 5 and 2 days, Figure 2.8. These observations, together with those for the wind stress field discussed above, point to the conclusion that the FNOC wind analyses *are* sensitive to coastal meteorological processes (associated with coastal topography, etc.) but do not necessarily represent them accurately (see Halliwell and Allen, 1986), and that wind stress curl computed from them contains spatial variability on scales of the FNOC grid spacing (~ 330 km at the latitude of this study). However, the $\nabla \times \tau$ time series will not *define* scales of this magnitude; more likely, wavelengths the order 1000 km will be resolved. A time series of wind stress curl over the OPTOMA domain is computed from wind stress at points G, K, and L for October 1984 to July 1985 (the interval of current meter data to be used in this study), Figure 4.3. The wind stress curl time series is filtered as described above for wind stress. The autospectrum of the wind stress curl has peaks centered at about 25, 12, 8, and 3 day periods, Figure 2.9. The spectrum falls off as $\sim \omega^{-3/2}$ (where ω is the frequency) for periods less than three days, which is consistent with the spectral character of $\nabla \times \tau$ selected by Frankignoul and Muller (1979) for model studies after examination of available wind and wind stress curl time series.

TABLE 3
FNOC WIND STRESS CURL MONTHLY MEANS
AND LONG TERM MEANS OF NELSON (1977)

| MONTH | PRESENT STUDY * | NELSON (1977) * |
|-----------------------------|-----------------|-----------------|
| OFFSHORE POINT (37N, 128W) | | |
| JUL | 0.5 | -0.3 |
| AUG | -0.8 | -2.1 |
| SEP | -0.3 | -0.2 |
| OCT | -1.0 | -1.1 |
| NOV | -0.5 | -0.9 |
| DEC | 1.6 | 0.0 |
| JAN | -0.4 | 0.8 |
| FEB | -0.3 | 0.5 |
| MAR | -0.4 | -1.7 |
| APR | -1.4 | -0.8 |
| MAY | -1.0 | -1.2 |
| JUN | 0.3 | -1.6 |
| NEARSHORE POINT (39N, 125W) | | |
| JUL | 4.8 | 1.3 |
| AUG | 1.4 | 1.6 |
| SEP | 1.9 | 1.9 |
| OCT | 0.3 | 3.3 |
| NOV | -1.7 | 3.0 |
| DEC | 1.4 | 0.0 |
| JAN | 1.1 | 0.2 |
| FEB | 2.1 | -1.5 |
| MAR | 0.6 | 1.5 |
| APR | 0.3 | 0.9 |
| MAY | 0.9 | -0.8 |
| JUN | 2.7 | 2.0 |

*: units are 10^{-8} dyn cm^{-3}

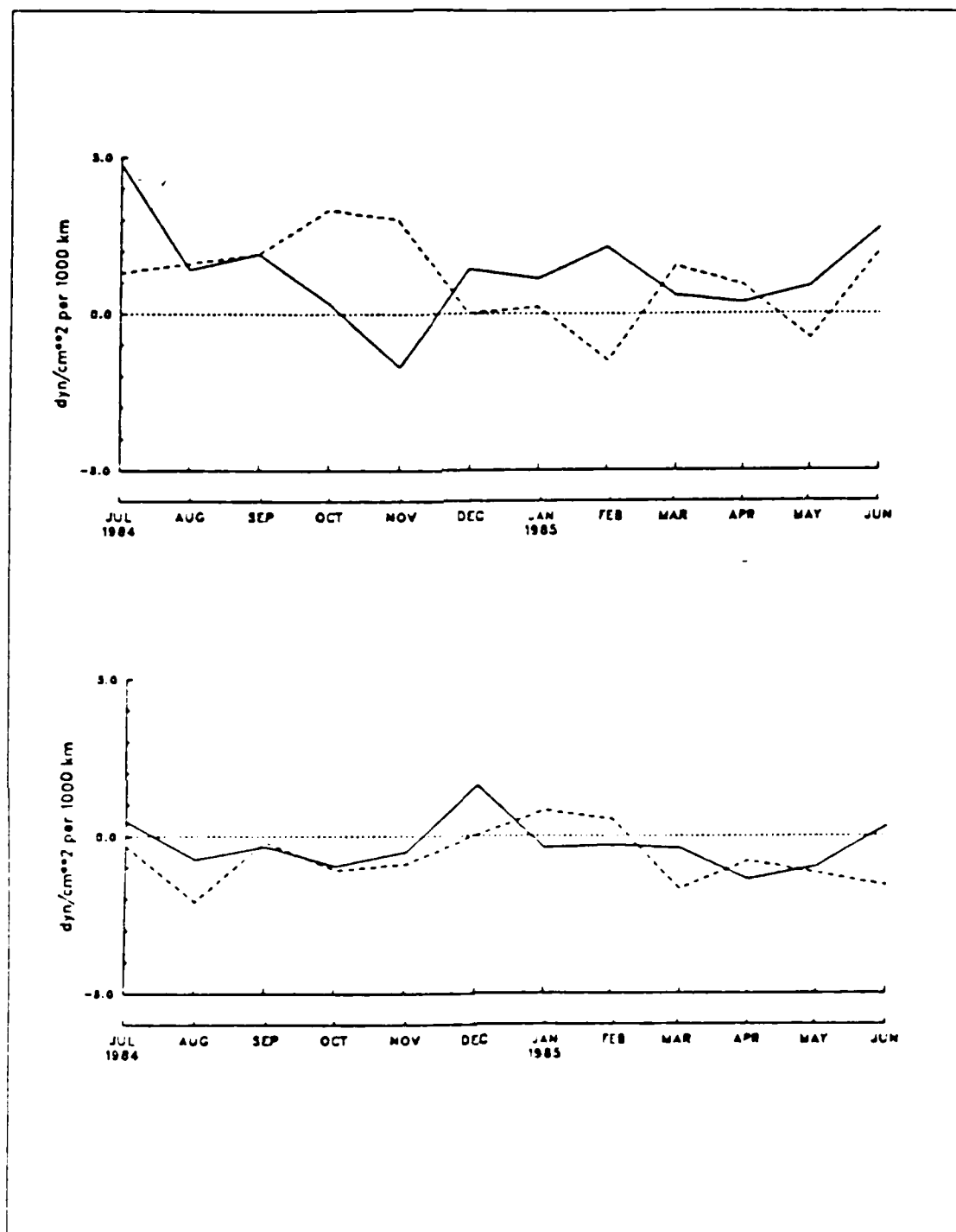


Figure 2.7 Comparison of wind stress curl monthly means for nearshore (top) and offshore (bottom) cases. Solid line: present study, dashed line: Nelson (1977).

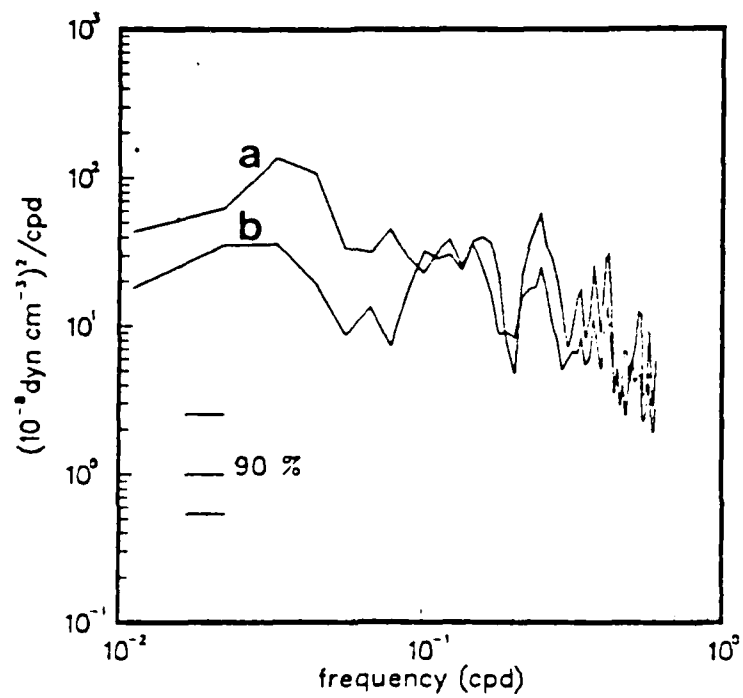


Figure 2.8 Wind stress curl spectra for nearshore (a) and offshore (b) cases.

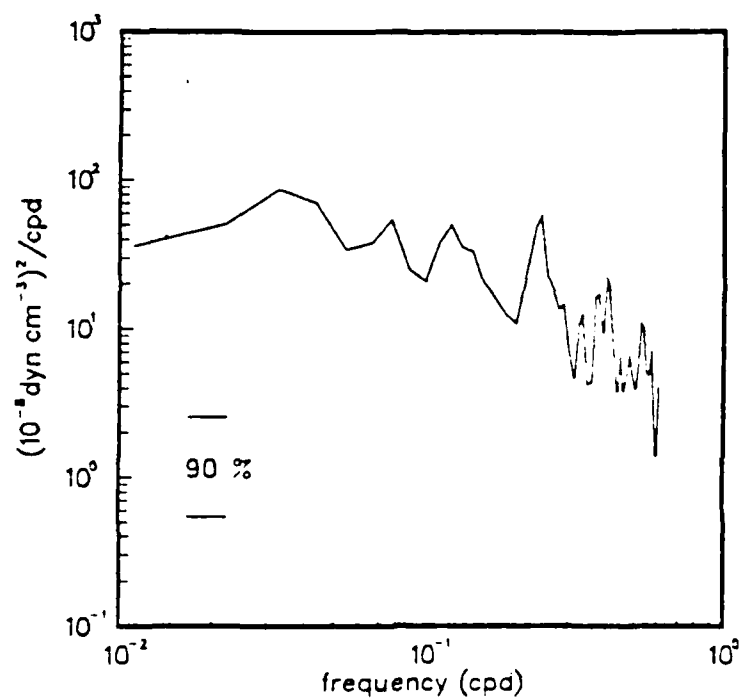


Figure 2.9 Autospectrum of wind stress curl over the OPTOMA domain for the period covering the current meter moorings.

III. THE CURRENTS

A. CURRENT DATA

The three OPTOMA current meter moorings were deployed off northern California from September 1984 to July 1985 by Prof. R.L. Smith at Oregon State University in association with the OPTOMA program. The moorings (designated M1, M2, and M3), Figure 3.1, were separated by about 100 km. Five Aanderaa current meters were installed on each mooring to record temperature, pressure, current speed and direction, at 1 hourly intervals. The deepest instrument at each mooring was approximately 200 m above the bottom. Calibration and post-processing were carried out at Oregon State University (Smith *et. al.*, 1986). Two meters each on moorings M1 and M3 failed or provided incomplete records. Hence, a total of 11 records from the three moorings are used for this analysis, Table 4.

The most comprehensive time overlap of the current records is 0400, 02 October 1984 to 2300, 02 July 1985 (inclusive) and, hence, this period is selected for the focus of study. All current records are low-pass filtered and then subsampled at six-hourly intervals. None of the current time series appear to be rotary in nature, Figures 3.2, 3.3, and 3.4. Means of all records are not statistically significantly different from zero at the 95% level, Table 5. The 95% significance level is given by the standard error:

$$2\sigma/N^{1/2},$$

where σ is the standard deviation and N is the number of degrees of freedom. Standard deviation ellipses, aligned so that the major axis is parallel with the direction of minimum Reynold's stress, show the maximum variance to be polarized in the north south direction. Monthly standard deviation exceeds monthly mean in all cases. There are large month-to-month variations in the mean direction as well as magnitude, but in all except a few cases the monthly mean is not significantly different from zero at the 95% level, Figure 3.5.

1. Autocorrelation Functions and Time Scales

A prominent signal with a period of ~ 70 days dominates the autocorrelation functions of the meridional components of M2-340 and M3-350, Figure 3.6, as for

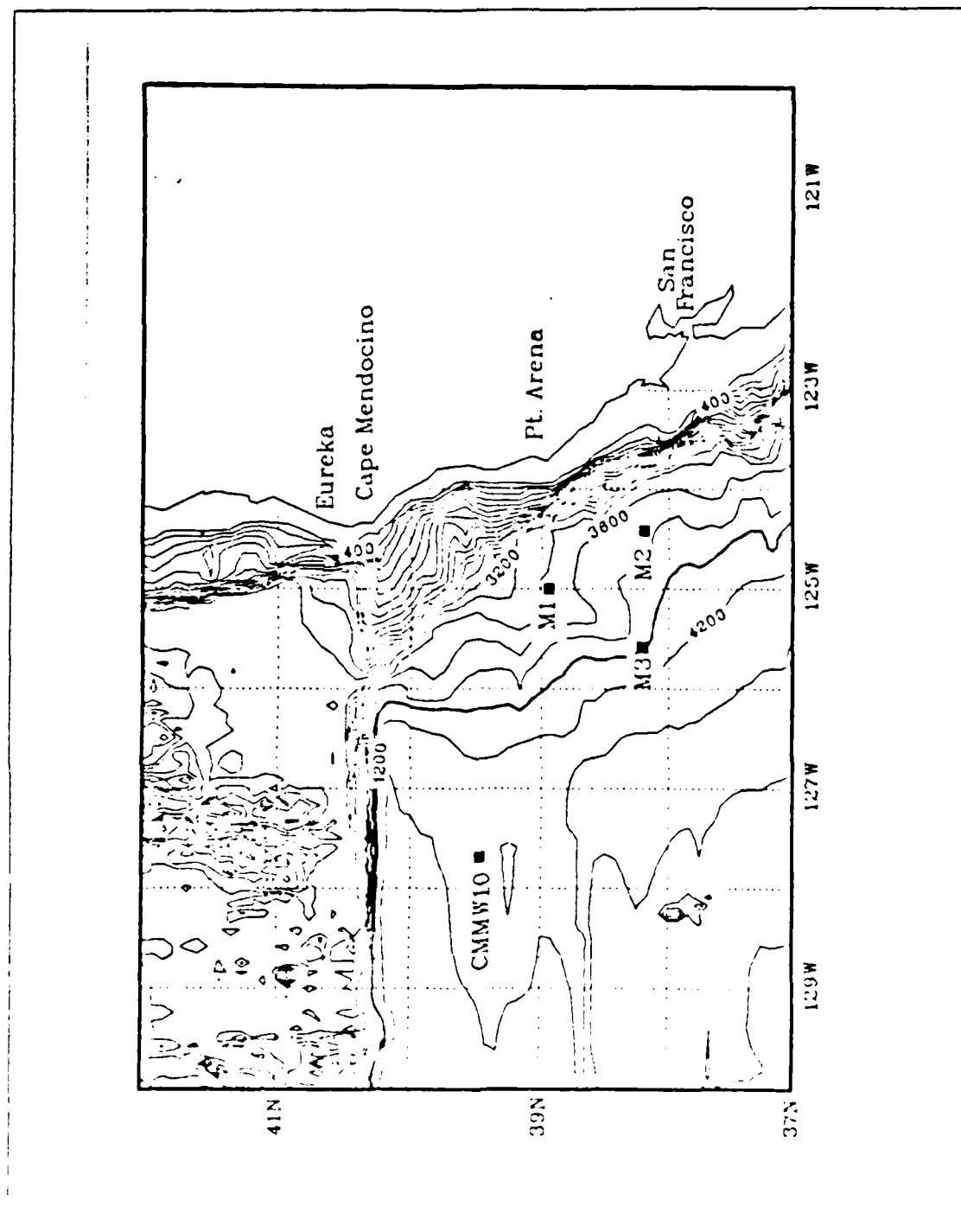


Figure 3.1. Locations of moorings M1, M2, M3, and CMMW10 with respect to bathymetry. Depths are in meters. Contour interval is 200 m.

TABLE 4
CURRENT METER DEPTHS AND RECORDED VARIABLES
USED IN ANALYSIS

| DEPTH (m) | VARIABLES |
|-------------------|------------------|
| MOORING M1 | |
| 175 | u,v,T |
| 375 | u,v,T |
| *3250 | u,v |
| MOORING M2 | |
| 145 | u,v,T |
| 340 | u,v,T |
| 800 | u,v |
| 1190 | u,v |
| *3560 | u,v |
| MOORING M3 | |
| 350 | u,v,T |
| 800 | u,v |
| 1185 | u,v |

LEGEND

u: Zonal velocity component
v: Meridional velocity component
T: Temperature
*: Denotes instrument ~ 200 m above bottom

many other levels except those near the bottom.¹ The autocorrelation function of the zonal component of M3-350 has a markedly longer dominant period than do those for M1-375 and M2-340, Figure 3.6. Decorrelation times for both components range from 2-to-22 days; smallest values are for the near-bottom records at M1 and M2 (Table 6). Integral time scales range from 4-to-38 days. Again, the smallest values are for the near-bottom records at M1 and M2, and for the u-components of M1-175 and M2-145.

¹M1-375 denotes the current record from M1 at 375 m depth. Other current meter records will be referred to in a similar manner.

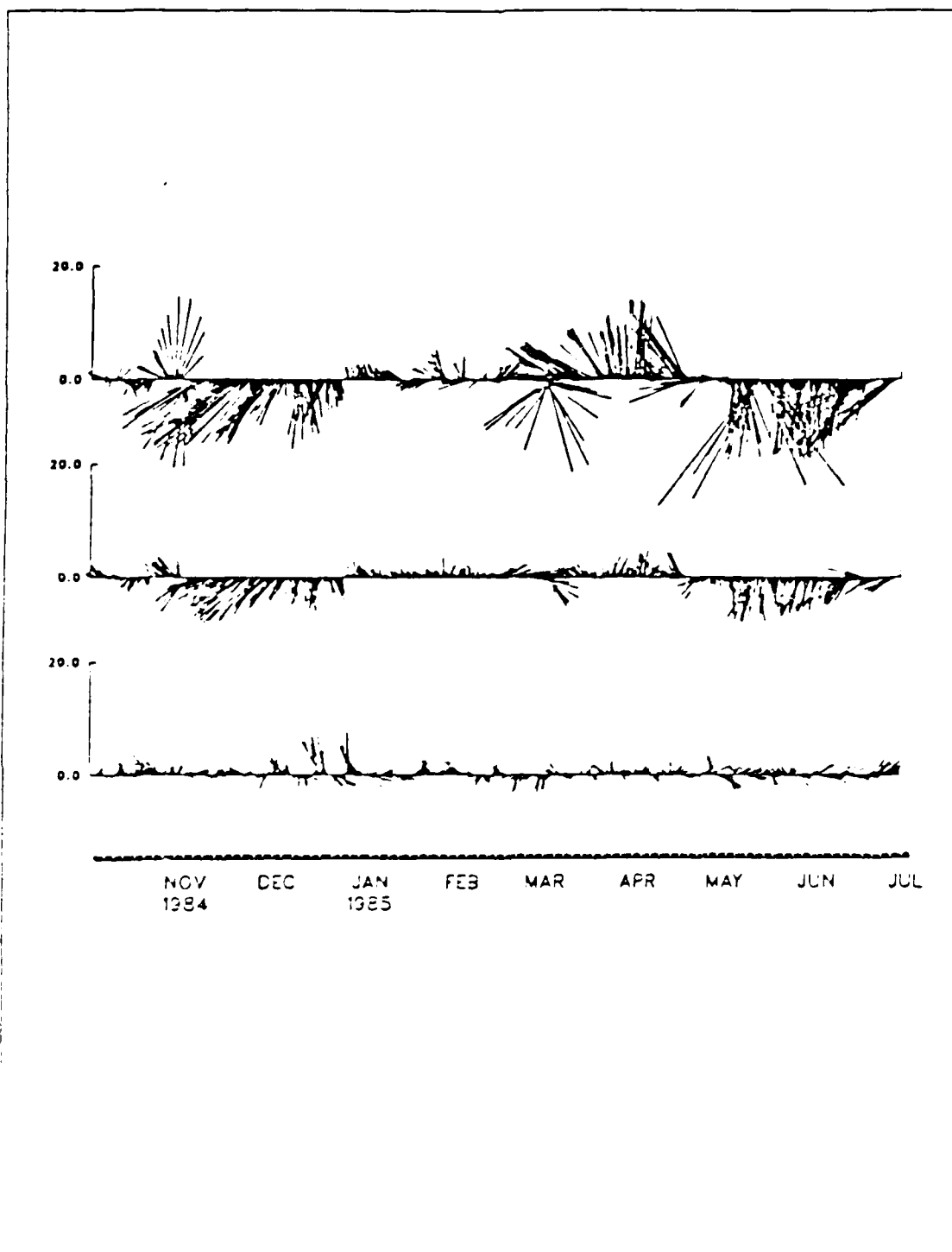


Figure 3.2 Current time series from mooring M1. Depths from top are 175, 375, and 3250 m. Units: cm/s.

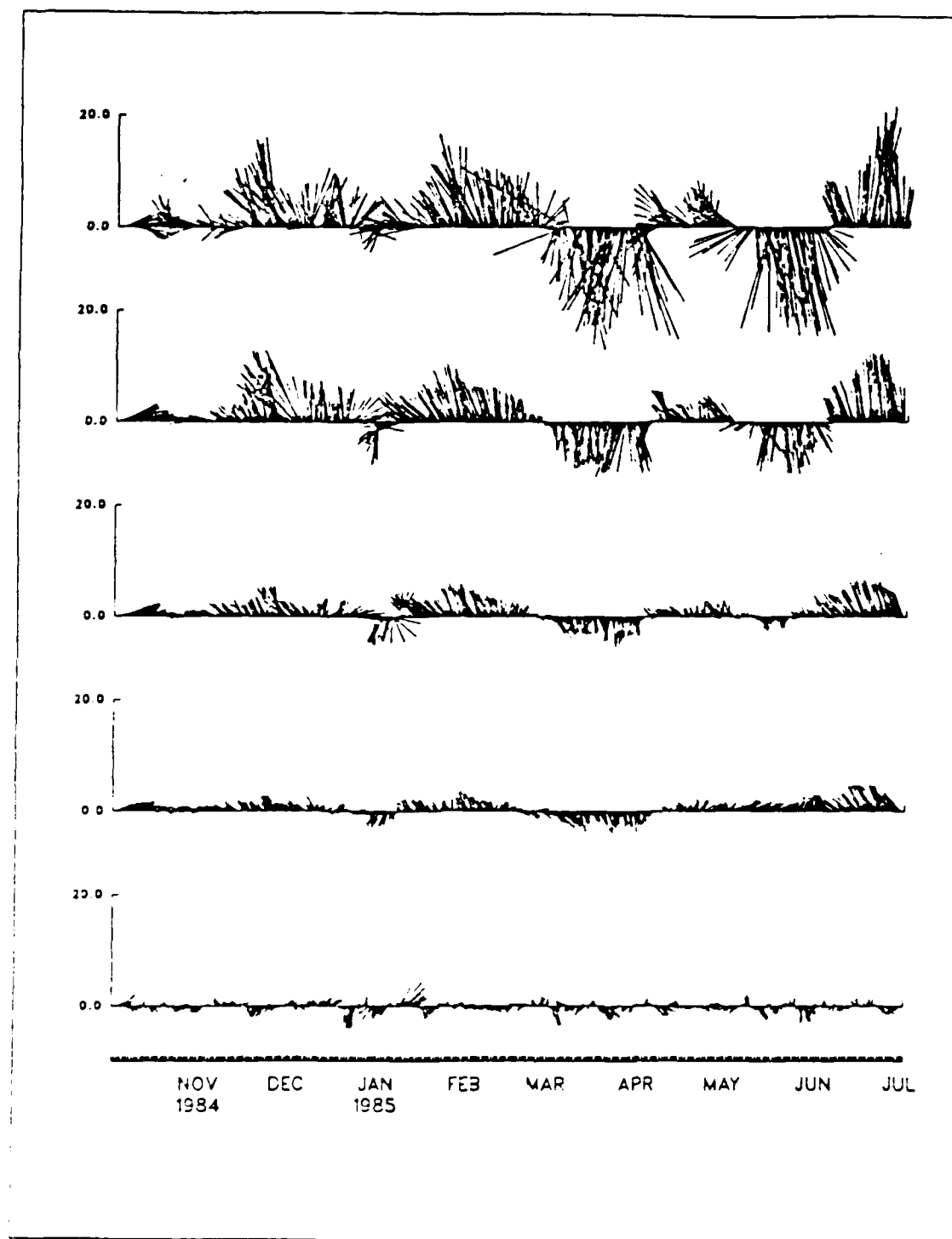


Figure 3.3 Current time series from mooring M2. Depths from top are 145, 340, 800, 1190, and 3560 m. Units: cm s.

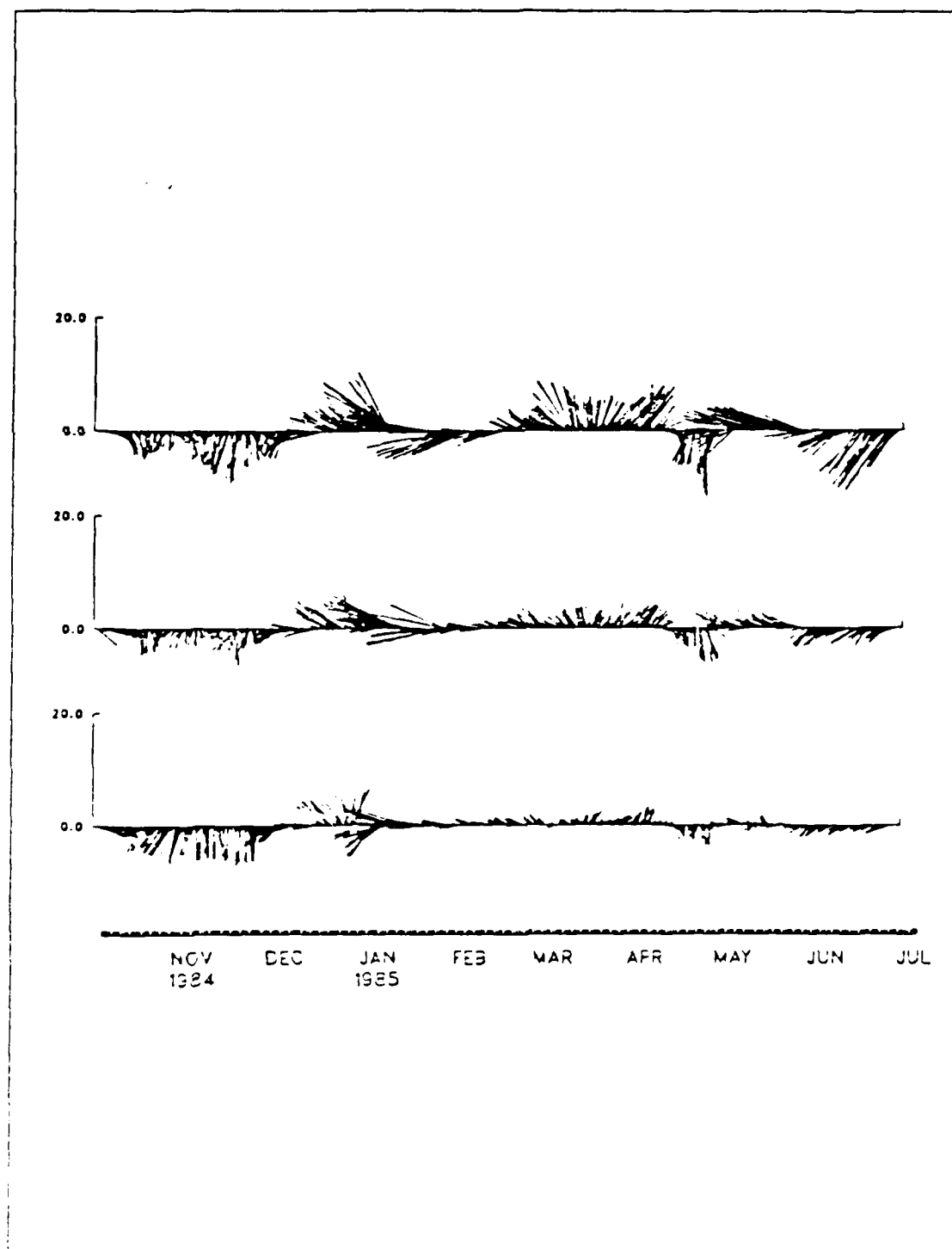


Figure 3.4 Current time series from mooring M3. Depths from top are 350, 800, and 1185 m. Units: cm s.

TABLE 5
STATISTICS OF CURRENT AND TEMPERATURE RECORDS

| RECORD | $\langle u \rangle^*$ | σ_u^* | $\langle v \rangle^*$ | σ_v^* | $\theta^\#$ | $\langle T \rangle^{**}$ | σ_T^{**} |
|---------|-----------------------|--------------|-----------------------|--------------|-------------|--------------------------|-----------------|
| M1-175 | -2.4 | 4.8 | -2.5 | 6.7 | 8 | 8.5 | 0.47 |
| M1-375 | -0.9 | 2.5 | -1.2 | 2.9 | 33 | 6.3 | 0.26 |
| M1-3250 | 0.2 | 1.3 | 0.4 | 1.5 | -27 | 1.5 | 0.06 |
| M2-145 | -1.4 | 3.7 | 1.0 | 8.9 | -6 | 8.4 | 0.47 |
| M2-340 | -1.0 | 2.5 | 1.5 | 5.4 | -9 | 6.2 | 0.35 |
| M2-800 | -0.5 | 1.8 | 1.1 | 2.6 | -22 | 4.2 | 0.11 |
| M2-1190 | 0.0 | 1.4 | 0.6 | 1.7 | -34 | 3.7 | 0.05 |
| M2-3560 | 0.0 | 0.9 | -0.3 | 1.1 | 10 | 1.5 | 0.01 |
| M3-350 | -3.5 | 4.6 | -0.6 | 4.4 | -59 | 6.3 | 0.38 |
| M3-800 | -2.4 | 3.4 | -0.1 | 2.3 | -74 | 4.2 | 0.13 |
| M3-1185 | -1.7 | 2.6 | -0.8 | 2.5 | -52 | 3.2 | 0.08 |

$\langle \rangle$: denotes mean

σ : denotes standard deviation

*: units: cm/s

**: units: °C

#: in degrees clockwise from north

2. Spectrum Analysis

The current records are processed and transformed for spectrum analysis as described for the wind records in Chapter II. The auto-rotary spectra of all the current records except the near-bottom records are similar. The spectra do not display distinctive rotary character, except at the lowest frequencies and some isolated higher frequencies ($\omega \sim 0.22$ cpd). At the lowest frequencies the clockwise component

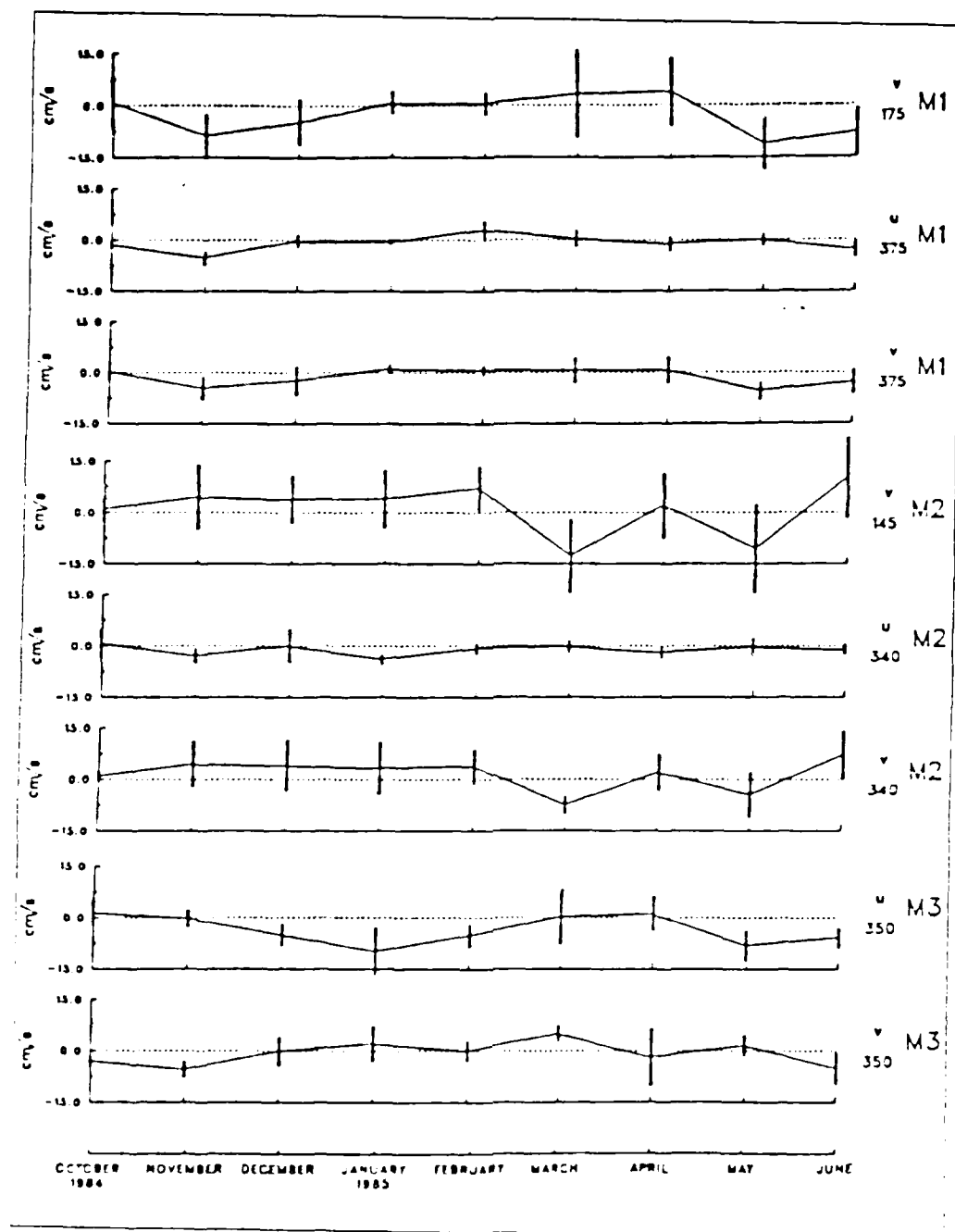


Figure 3.5 Monthly mean and standard error of selected current records at M1, M2 and M3. Units: cm/s.

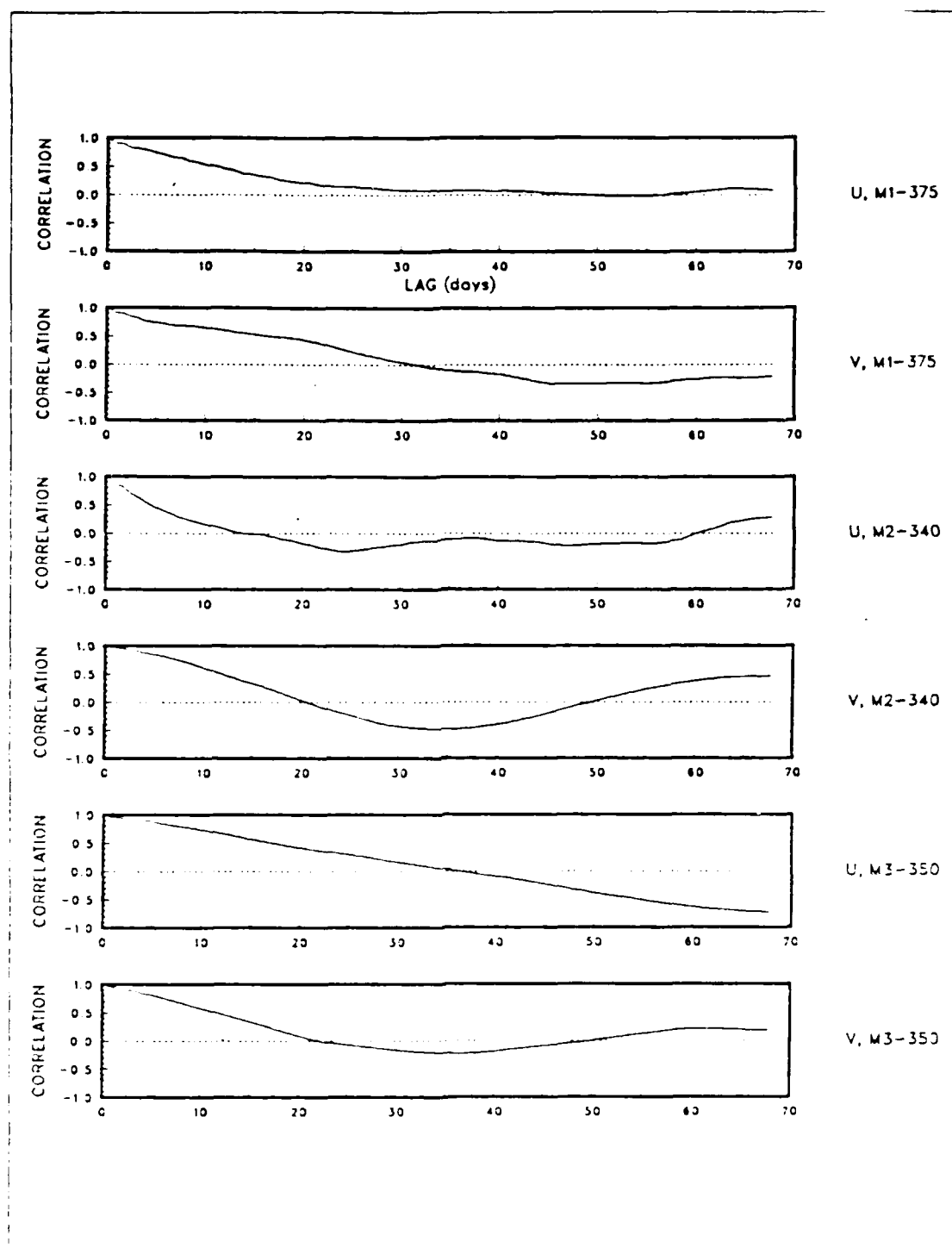


Figure 3.6 Autocorrelation functions of zonal and meridional components of M1-375, M2-340, and M3-340.

TABLE 6
INTEGRAL TIMES SCALES AND DECORRELATION
TIMES FROM CURRENT RECORDS

| DEPTH (m) | INT. TIME SCALE * | | DECORR. TIME * | |
|-------------------|-------------------|----|----------------|----|
| | u | v | u | v |
| <i>MOORING M1</i> | | | | |
| 175 | 9 | 21 | 8 | 21 |
| 375 | 15 | 24 | 14 | 22 |
| 3250 | 6 | 6 | 3 | 2 |
| <i>MOORING M2</i> | | | | |
| 145 | 5 | 26 | 4 | 13 |
| 340 | 10 | 28 | 6 | 14 |
| 800 | 17 | 20 | 9 | 13 |
| 1190 | 17 | 19 | 14 | 18 |
| 3560 | 4 | 4 | 3 | 2 |
| <i>MOORING M3</i> | | | | |
| 350 | 38 | 18 | 22 | 14 |
| 800 | 32 | 12 | 22 | 12 |
| 1185 | 28 | 18 | 17 | 21 |

*: units are days

dominates; at $\omega \sim 0.22$ cpd the anticlockwise component is more energetic. The spectra are red to $\omega \sim 0.3$ cpd and essentially white at higher frequencies, Figure 3.7.

The spectrum of M1-3250 is white for $\omega < 0.05$ cpd and $\omega > 0.15$ cpd. There is a large amplitude peak in the spectrum (both rotary components) centered at $\omega \sim 0.1$ cpd, Figure 3.8. The M2-3560 spectrum is essentially white to about 0.1, decreases sharply by about an order of magnitude, and is white at $\omega > 0.2$ cpd, Figure 3.9.

3. Dynamical Mode Decomposition

The current field dynamical modes are shown for completeness, Figure 3.10, since they are used in analysis of the current response to wind forcing in Chapter IV. The current field is decomposed into dynamical modes using a Brunt-Vaisala frequency profile, $N^2(z)$, computed from an average of OPTOMA CTD casts within ~ 50 km of the moorings (Rienecker *et. al.*, 1986).

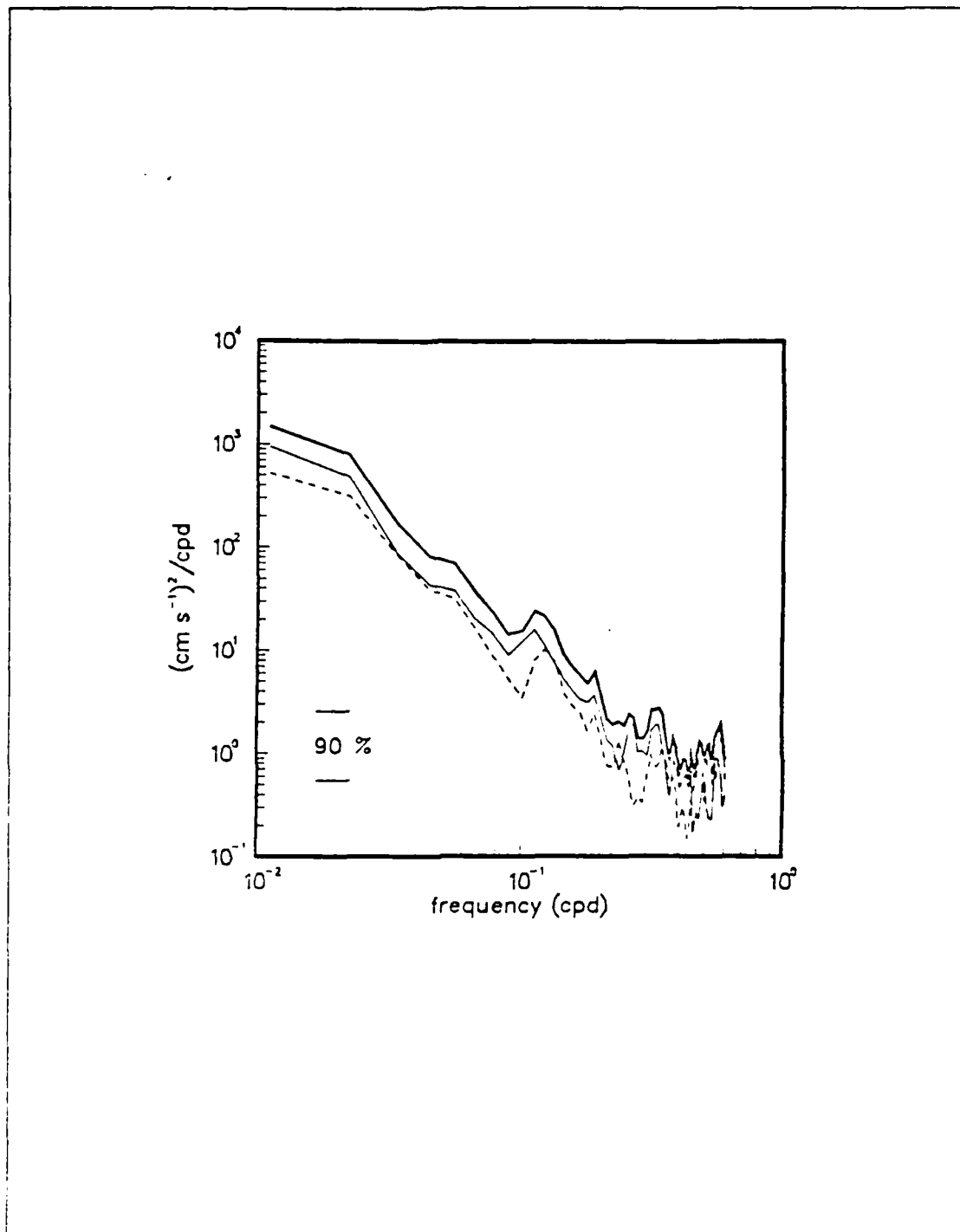


Figure 3.7 Auto-rotary spectra of current at M2-340, (typical of other records). Thick line: total spectrum; dashed line: anticlockwise, thin line: clockwise.

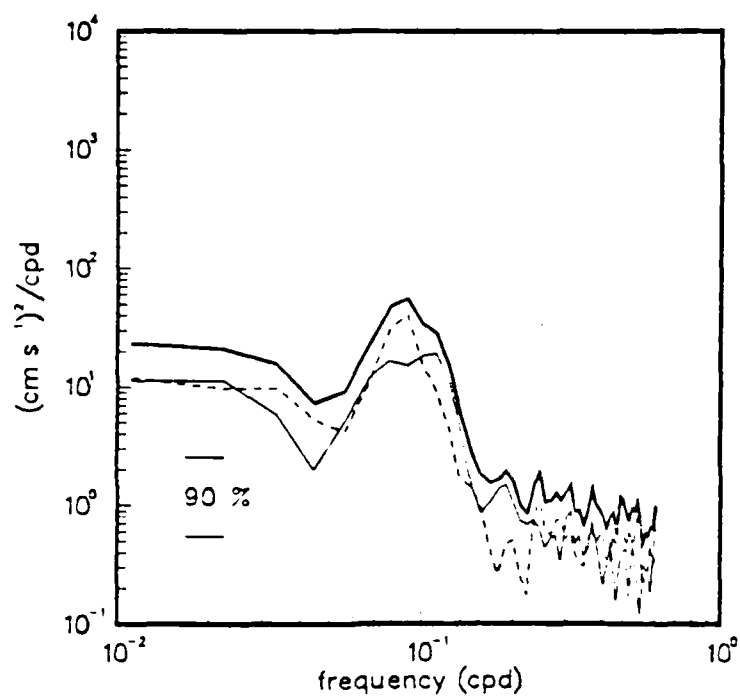


Figure 3.8 As in Figure 3.7, but for M1-3250.

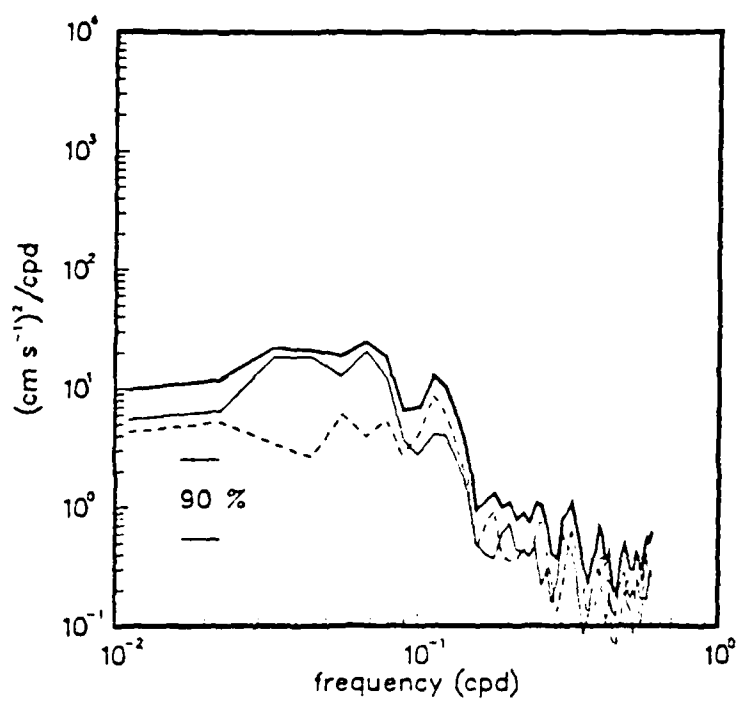


Figure 3.9 As in Figure 3.7, but for M2-3560.

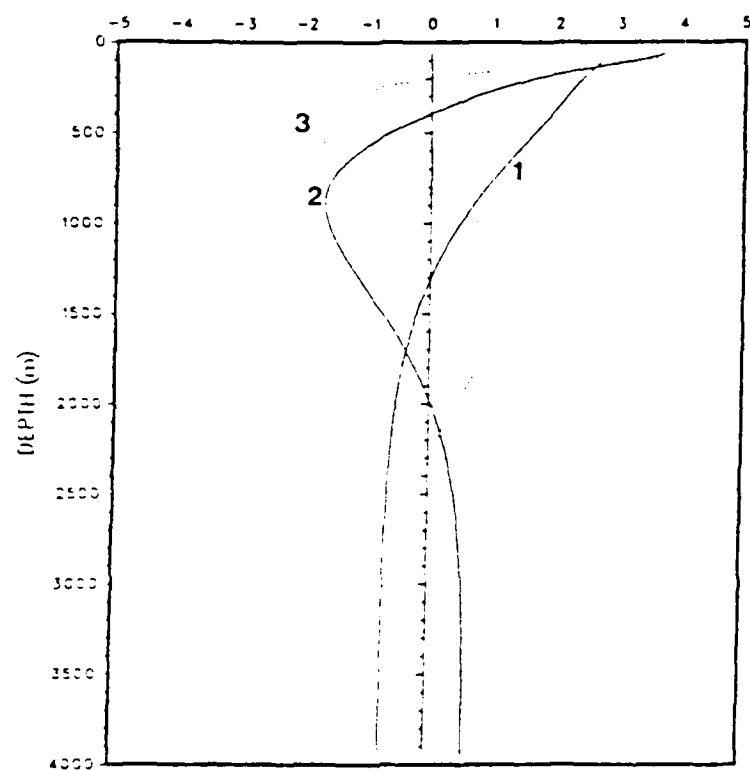


Figure 3.10 First three baroclinic normal modes computed from CTD casts within 50 km of M1, M2, and M3.

B. SPATIAL VARIABILITY OF CURRENTS

1. *Vertical Coherence*

Planar cross-spectra of all the pairs of meridional current components at mooring M2 are computed to investigate the vertical coherence of the flow. The coherence of each pair at a period of 45 days is computed and compared to the coherence of the other pairs as a function of vertical separation (Δz), Figure 3.11. At low frequency, the coherence generally decreases with increasing Δz at mooring M2, Figure 3.11. This variability, also found at M1 and M3, contrasts sharply with the nearly barotropic flow found by Niiler and Koblinsky (1985) much farther offshore and north of the Mendocino Escarpment (42N, 152W), and suggests a much more complicated flow structure in the OPTOMA domain than for "open ocean" regimes.

2. *Horizontal Coherence*

The only meters at a common depth between the three moorings that are available to investigate horizontal variability are those at about 350 m. The planar cross-spectra of the principal axis components are computed as a measure of the horizontal coherence of the flow. M1 and M2 are coherent² only at 8-9 day periods, and M1 is coherent with M3 only at very short (<3 day) periods. M2 and M3 are coherent for periods longer than ~ 40 days, Figure 3.12. Hence, there is limited coherence between all three moorings at the 350 m level, but at different periods for each pair. The moorings are located in an area of complex bottom topography, Figure 3.1, which presumably accounts for the general lack of horizontal coherence in the current field.

²Unless otherwise indicated, the 90% significance level will be used throughout for coherence no coherence determinations.

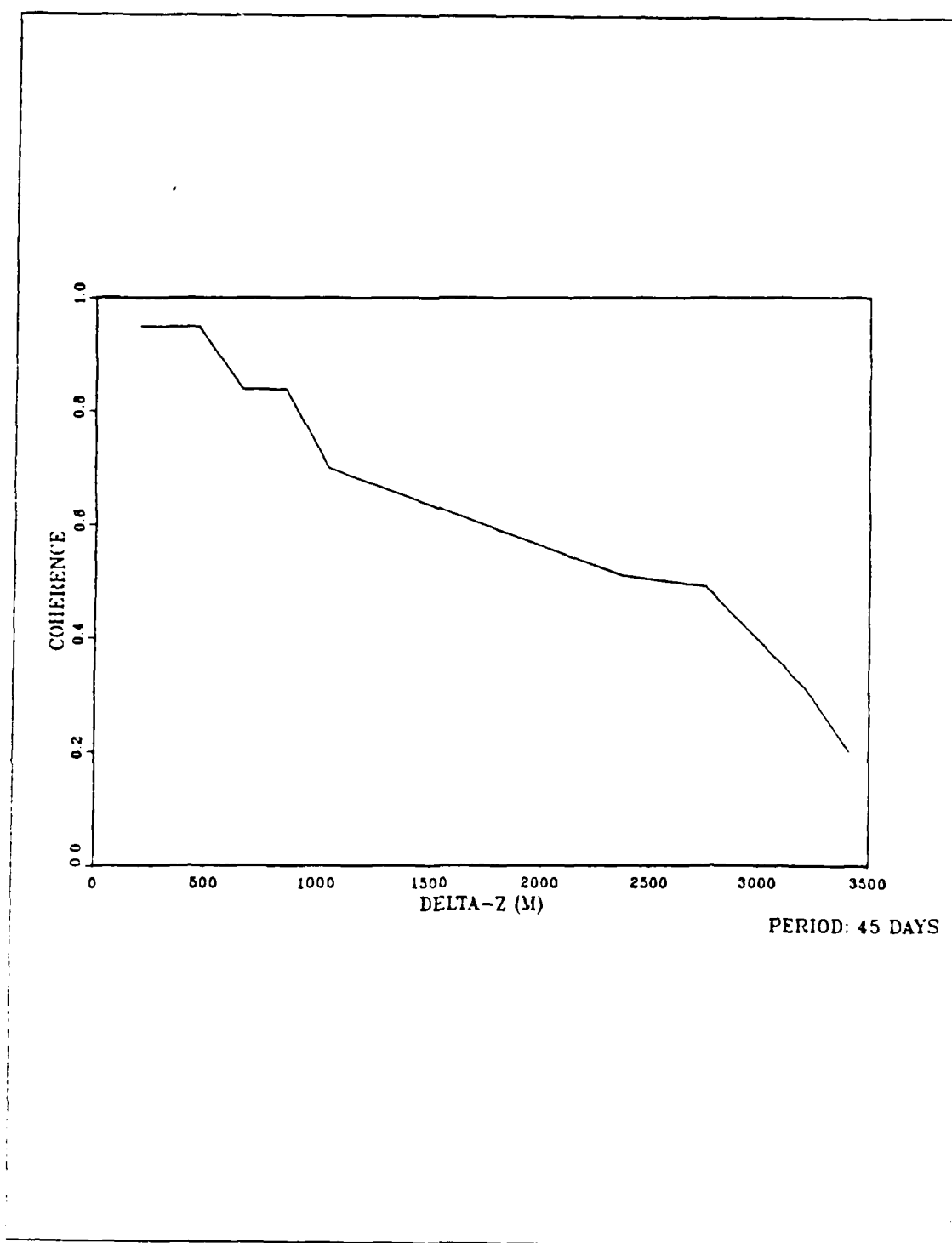
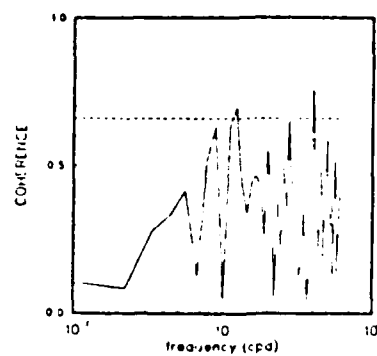
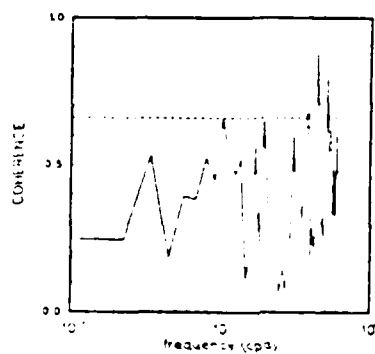


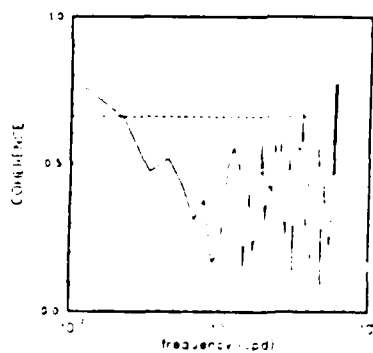
Figure 3.11 Coherence between pairs of meridional current components at M2 as a function of vertical separation (ΔZ).



M1-375 AND M2-340



M1-375 AND M3-350



M2-340 AND M3-350

Figure 3.12 Coherence between current components parallel to the principal axis direction of M1-375, M2-340, and M3-350.

IV. THE CURRENT RESPONSE TO WINDS

Theoretical studies and model results (e.g., Muller and Frankignoul, 1981 and Willebrand *et. al.*, 1980) suggest that the relationship between atmospheric forcing and the open oceanic response is complex and not readily observable. Muller and Frankignoul (1981) compared model results to observations for an open ocean (weak eddy field) regime. Their results suggest that atmospheric forcing may be the dominant energy source for geostrophic eddies in regions removed from strong currents. They concluded, however, that direct evidence of this may be difficult to establish, especially at low frequency. Willebrand *et. al.* (1980) used wind data derived from synoptic NMC surface pressure charts to force a closed-basin numerical model. From the barotropic vorticity equation for a flat-bottom ocean, they concluded that the oceanic response to stochastic atmospheric forcing is characterized by three distinct frequency ranges:

- At periods of 1 to 10 days the response is locally forced.
- At periods of 10 to 30 days the response is in the form of planetary waves.
- At periods longer than a month the motion corresponds to a Sverdrup balance.

Their results from a nonlinear numerical model forced by realistic winds confirmed this conclusion. They also found that bottom topography significantly altered coherence between the ocean and atmospheric forcing. Their conclusion that the Sverdrup balance dominates only at periods greater than 30 days contrasts with the results of Niiler and Koblinsky (1985), who found evidence of a time-dependent Sverdrup balance at periods of 10-100 days.

The cross-spectra of wind and current meter records described in Chapters II and III are analyzed seeking:

- coherence between ocean currents and wind stress in each of the frequency bands defined by Willebrand *et. al.* (1980)
- evidence of Ekman pumping
- evidence of the Sverdrup balance
- other factors that may selectively mask the oceanic response to wind forcing in frequency, space, or time.

It is anticipated that this regime is different from those previously investigated. It is near (100-200 km) the coast, yet probably too far offshore to observe coastal effects

such as coastally trapped waves. On the other hand, it is clearly *not* analogous to the open ocean regimes studied by numerous earlier investigators. The bottom topography in the study area is very complicated, Figure 3.1. It is anticipated that this will tend to destroy (or cover) coherence between the ocean and wind forcing.

A. WIND STRESS/CURRENT CROSS-SPECTRUM ANALYSIS

For consistency, wind stress at point G will be used for all wind/current cross-spectrum analyses using the OPTOMA current data. Point G is closest to all of the mooring locations, Figure 2.1. Standard deviation ellipses of points K and L are larger than that of point G, Figure 4.1, reflecting their position closer to the storm track across Oregon and northern California. Since the moorings are somewhat south of the storm track, point G wind stress is probably more representative of the actual wind over the moorings. The orientation of the standard deviation ellipse for point G is steadier with frequency than those for points K and L and is aligned $\sim 15^\circ$ west of north, Figure 4.1. This alignment is consistent with the wind direction that is expected on the downstream side of the North Pacific subtropical high (see Chapter I). The standard deviation ellipses of points K and L are aligned east of north and, hence, not consistent with the wind flow expected around the subtropical high, Figure 4.1. Cross-spectra of wind stress at points G, K, and L with several current records show point G to be the most coherent with current records. In several ways, then, wind stress at point G appears to be the most representative of wind stress over the OPTOMA moorings and is selected over points K and L. All further references to wind stress will be to wind stress at point G unless otherwise noted.

The wind stress principal axis direction is aligned about 15° west of north and is nearly constant with frequency, especially over portions of the spectrum where ellipse stability is high. Neither the wind stress nor any of the current time series is significantly rotary in nature, so the planar cross-spectra of τ_x vs. u and τ_y vs. v are computed. The planar cross-spectra have many coherent peaks, but more for the τ_y vs. v cases than for the τ_x cases (probably since τ_y is more energetic than τ_x). Table 7. There are coherent peaks in the "locally forced" band (periods of 1-10 days) in each of these cross-spectra, except τ_y vs. v at M2-800. These peaks are concentrated at periods of 3-9 days, Table 7. There is very little coherence in the "planetary wave" band (10-30 day periods); M1-175 and M1-3250 for the τ_y vs. v case and M2-145 for the τ_x vs. u case are the only ones with coherence in this band. There is coherence between wind

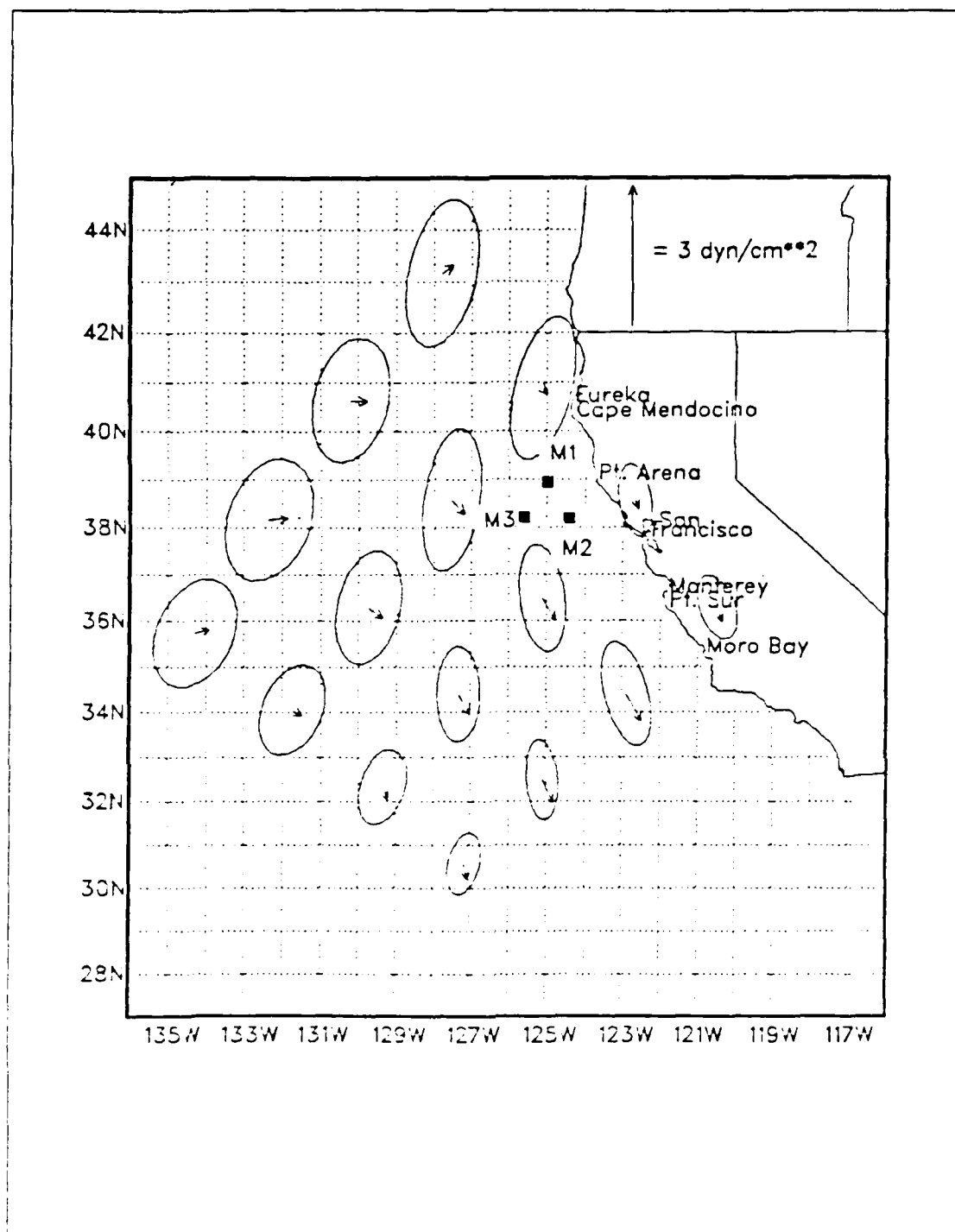


Figure 4.1 Mean vectors and standard deviation ellipses for wind stress at FNOC grid points A through P over the period of the study.

stress and current components in the "Sverdrup balance" band (< 30 day periods) for several of the cases, Table 7.

TABLE 7
COHERENT PEAKS BETWEEN WIND STRESS AND
CURRENT COMPONENTS

| MOORING/DEPTH (m) | PERIODS OF COHERENT PEAKS (days) | |
|-------------------|----------------------------------|------------------|
| | τ_x vs. u | τ_y vs. v |
| M1-175 | 7* | 5.5, 10, 15, 22 |
| M1-375 | 3.5*, 7* | 7*, 9 |
| M1-3250 | 4, 7 | 5*, 6.5*, 9, 15 |
| M2-145 | 4*, 8*, 24* | 3.3, 5*, 9, > 45 |
| M2-340 | 15 | 5, 9, > 45 |
| M2-800 | 3.3 | 43-71 |
| M2-1190 | 5 | 9, 43-55 |
| M2-3560 | 6* | 8* |
| M3-350 | 5*, 7*, 45* | 9 |
| M3-800 | 3.5*, 4.5, 5, 45 | 5*, 10* |
| M3-1185 | 3.5 | 9* |

*: coherence exceeds 95% level

The current components parallel to the principal axis direction for M1-375, M2-340, and M3-350 are designated M1-375₊₃₃, M2-340₋₁₀, and M3-350₋₆₀, where the subscript denotes the principal axis direction in degrees clockwise from north. M1-375₊₃₃ is coherent with τ_y at a period of ~ 8 days. M2-340₋₁₀ has coherent peaks with τ_y at 5.5 and 9 day periods, and for all periods greater than 45 days. There is significant coherence between τ_y and M3-350₋₆₀, especially at a period of 9 days, Table 8. In general, computation of cross-spectra using current and wind stress components parallel with their respective principal axis directions does not appreciably

affect the character of observed coherences from those in Table 7. As with the zonal meridional cross-spectrum analysis described above, there is evidence of ocean response to wind forcing at periods of 1-10 days, at periods of 10-30 days, and at long (> 30 days) periods. Higher frequency coherence (periods < 10 days) is consistently present in cross-spectra computed, intermediate frequency coherence is present in only one case, and lower frequency coherence (period > 30 days) is present in only one case. This is consistent with the results of Muller and Frankignoul (1981), who expected ocean wind coherence to be small and difficult to observe in the more energetic lower frequencies because of destructive interference of different wavenumbers, and with Willebrand *et. al.* (1980), who expected to find no coherence in the 10-30 day period band.

TABLE 8
COHERENT PEAKS BETWEEN WIND STRESS AND CURRENT
PARALLEL TO PRINCIPAL AXIS DIRECTION

| MOORING/DEPTH (m) | PERIODS OF COHERENT PEAKS (days) |
|-------------------|----------------------------------|
| M1-375 +33 | 4.3, 7.5*, 10, 15 |
| M2-340 -10 | 5.5, 9, > 45 |
| M3-350 -60 | 4.5*, 5, 5.5, 9* |

*: coherence exceeds 95% level

B. CROSS-SPECTRUM ANALYSIS WITH WIND STRESS CURL

1. Wind Stress Curl Versus Temperature and its Time Derivative

The cross-spectrum of wind stress curl with temperature records is computed, seeking evidence of Ekman pumping. $\nabla \times \tau$ is coherent with temperature at M1-375 for 14 and > 67 day periods, and with temperature at M2-340 for 18 and > 67 day periods. Temperature at M3-350 is coherent with $\nabla \times \tau$ for 6 and 28 day periods (the 28 day peak is significant at the 95% level). Essentially no coherence is found between $\nabla \times \tau$ and temperature records at any other level, but the coherence found at the 350 m level may be evidence of the Ekman pumping mechanism.

The heat equation may be expressed as:

$$\frac{\partial T}{\partial t} = -w \frac{\partial T}{\partial z} - \mathbf{u} \cdot \nabla T + K^2 \nabla^2 T + \frac{Q}{\rho c_p},$$

(1) (2) (3) (4) (5)

where term (1) is the local time derivative of temperature, (2) is vertical advection, (3) is horizontal advection, (4) is diffusion, and (5) is diabatic heating. If terms (3) through (5) can be assumed small and ignored, the local time derivative of temperature ($\partial T / \partial t$) may be taken as a measure of vertical velocity, w , which is related to wind stress curl by

$$w = \frac{1}{\rho} \nabla \times (\tau / f),$$

where ρ is the water density, f is the coriolis parameter, and τ is the wind stress. Usually the spatial variation of wind stress is greater than the variation of the coriolis parameter with latitude, so vertical velocity may be approximated as

$$w = (1/\rho f) \nabla \times \tau.$$

Thus, the Ekman pumping vertical velocity is proportional to the wind stress curl (Gill, 1982).

The cross-spectrum of wind stress curl and $\partial T / \partial t$ derived from the ~ 350 m temperature records at all three moorings, and from the shallow and deep temperature records at M1 and M2 are computed. $\nabla \times \tau$ is coherent with $\partial T / \partial t$ at M3-350 for periods of ~ 30 days and 8-9 days. At M1-375 and M2-340 there is no significant coherence with $\nabla \times \tau$ for any period. $\nabla \times \tau$ has a coherent peak with $\partial T / \partial t$ at M1-3250 for 14-day period. There are also a few peaks at high frequency (< 3 day period) for M1-175, M1-3250, M2-145, and M2-3560. The general lack of coherence between wind stress curl and $\partial T / \partial t$ suggests the importance of the neglected terms in the heat equation, especially (in this region) horizontal advection.

2. Wind Stress Curl and Temperature Versus Current Horizontal Divergence

Horizontal divergence is computed from the 350 m current at all three moorings. The current horizontal divergence spectrum is red at low frequency, has a peak at 10-day period, and becomes white for periods < 5 days.

Wind stress curl and horizontal divergence are coherent at periods of about 5 and 8 days. There is another smaller peak at high frequency (in the "weather" band), Figure 4.2, but in general there is little coherence between $\nabla \times \tau$ and horizontal divergence. The $\nabla \times \tau$ time series is much noisier than the horizontal divergence time series, and no correlation between the two is readily apparent, Figure 4.3. Similarly, there is very little coherence between temperature at any of the ~ 350 m records and horizontal divergence, and no apparent correlation between any of them and horizontal divergence, Figure 4.3.

Since the expected coherence between horizontal divergence and temperature is not found, an alternate hypothesis is proposed. If alongshore convergence between M1 and M2 at 350 m were to be accompanied by offshore flow (toward M3) of the same magnitude, then the horizontal divergence computed between M1, M2, and M3 would be small. Thus, significant alongshore convergence/divergence would necessarily not be reflected in the total horizontal divergence. There are several alongshore convergence events that are followed in time by a cooling event at M3-350 (~ 100 km farther offshore), Figure 4.3, and several examples of the opposite (alongshore divergence leading a warming event offshore). Alongshore divergence and temperature at M3-350 are coherent for periods greater than about 26 days, Figure 4.4. Their phase (with alongshore divergence leading temperature at M3-350) increases with increasing period (at periods for which they are coherent) and is greater than 180° , which is consistent with advection in the offshore direction. This is an indication that advection is an important process affecting variability in the study area, at least in the upper 350 m of the water column. This coherence is consistent with the CCS current filaments extending offshore, and to depths of 350 m that were described by Mooers and Robinson (1984) and Ikeda and Emery (1984).

3. *The Sverdrup Balance*

The Sverdrup balance in the presence of bottom topography is given by

$$\mathbf{U} \bullet \nabla(fH) = (\rho H)^{-1} \nabla \times \tau,$$

where \mathbf{U} is the horizontal current vector, H is the depth of the ocean, and ∇ is the two-dimensional horizontal gradient operator. This balance relates the current component across potential vorticity (fH) contours to local wind stress curl. To seek evidence of this balance, the cross-spectrum of wind stress curl with 350 m current components varied by 30° are computed to determine the direction of maximum

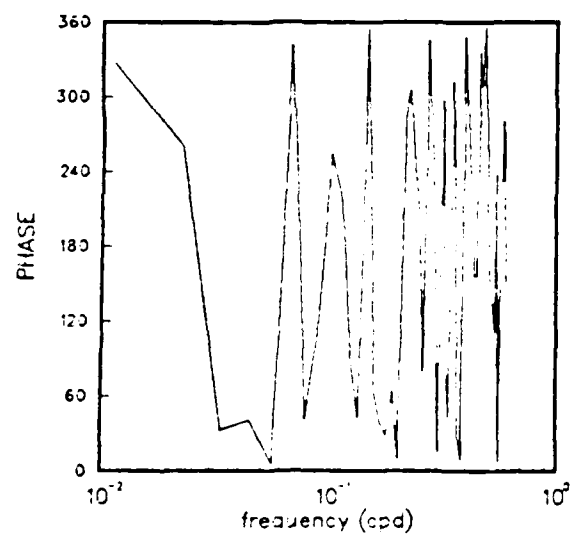
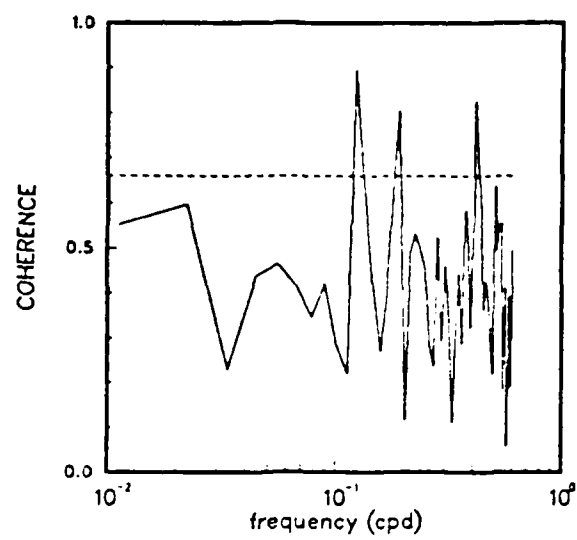


Figure 4.2 Coherence and phase between wind stress curl and horizontal current divergence at 350 m.

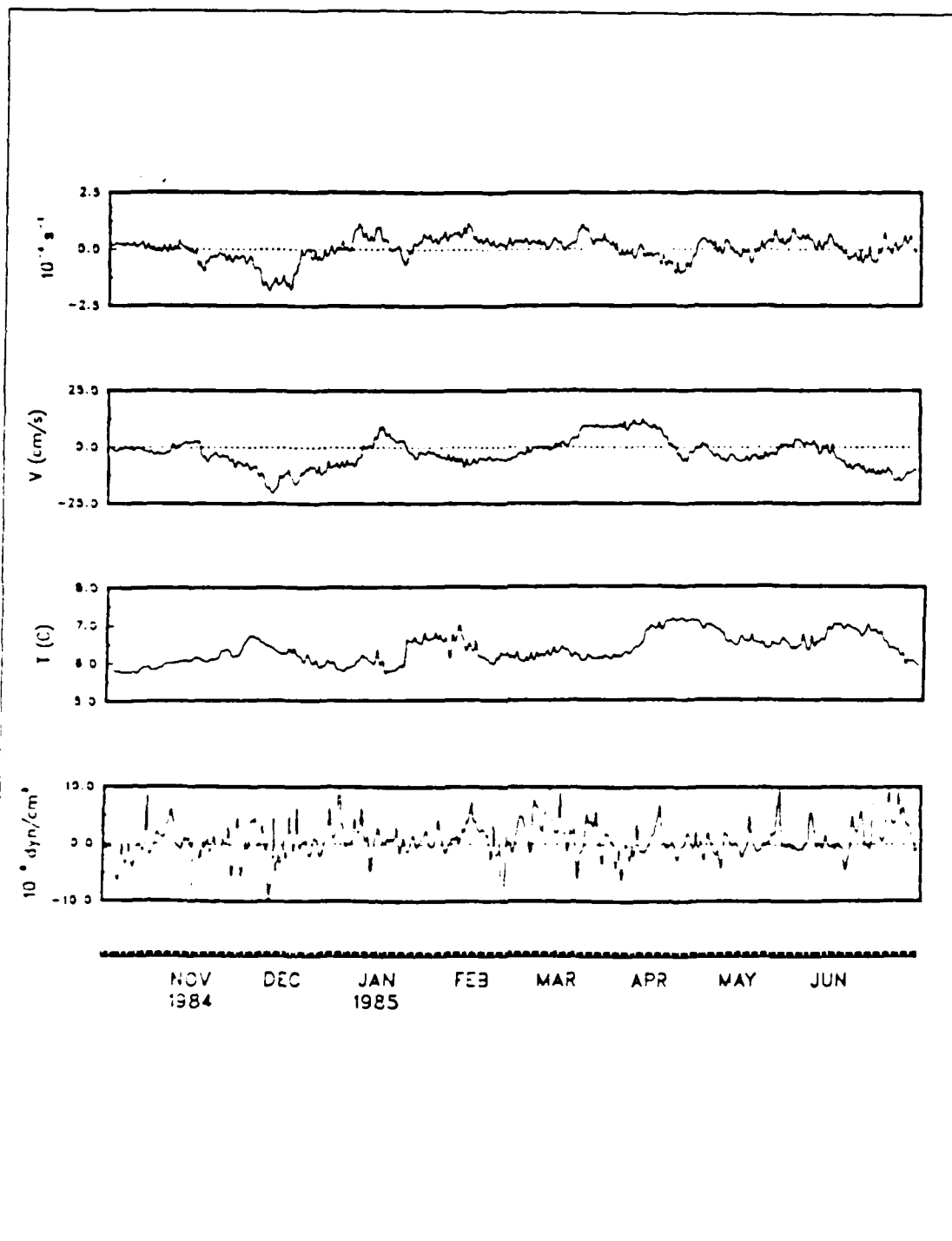


Figure 4.3 Time series of (from the top) horizontal divergence, alongshore divergence, temperature at M3-350, and $\nabla \times \mathbf{v}$.

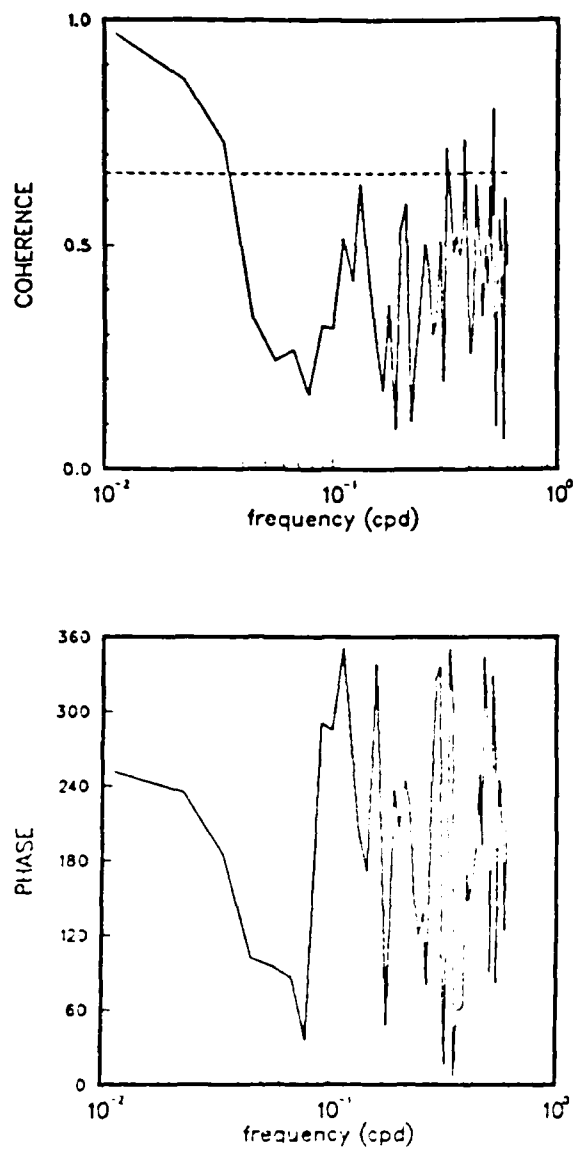


Figure 4.4 Coherence and phase between alongshore divergence (from M1 and M2) and temperature at M3-350.

coherence for each mooring. For M1-375, 30° east of north is the direction of maximum coherence - not inconsistent with the direction of the local bathymetric gradient, Figure 3.1. Wind stress curl is coherent with current parallel to $\nabla(f/H)$ at M1 for periods of 18 and 28-50 days, Figure 4.5. Wind stress curl and M2-340 (with current component 120° east of north) are coherent only at 90 days - this is not strong evidence for a Sverdrup balance, Figure 4.6. Wind stress curl is incoherent with M3-350 current components of any orientation.

C. WIND STRESS/DYNAMICAL MODE CROSS-SPECTRUM ANALYSIS

Component-wise cross-spectra of wind stress with current dynamical mode amplitudes are computed to investigate separately the barotropic and baroclinic ocean response to wind forcing.

1. Mooring M1

The meridional component of the barotropic mode is coherent with τ_y at periods of <3, 5, 6.5 and 10 days, Figure 4.7. The v-component of the first baroclinic mode has a large coherent peak with τ_y at a period of 15 days and a small peaks at 6.5 and 3-4 days, Figure 4.8. Hence, both modes share a coherent peak with τ_y at 3-4 days and at 6.5-day period. At lower frequencies, both modes are coherent with the wind forcing, but at decidedly different frequencies.

2. Mooring M2

The v-component of the barotropic mode and τ_y have coherent peaks at isolated periods <5 days and centered at 8 days. They are also coherent over periods greater than 55 days (just barely at the 90% level), Figure 4.9. The v-component of the first baroclinic mode is coherent with τ_y at periods <5 days and >55 days. It also has a coherent peak centered at 5 days, Figure 4.10. Hence, both dynamical modes are coherent with τ_y at short and long periods, but respond to τ_y at different intermediate frequencies. These intermediate frequencies are different from those at M1.

D. DISCUSSION

Zonal and meridional wind stress components are coherent with their corresponding current components at various periods in all three frequency bands defined by Willebrand *et. al.* (1980). The same is true of wind and current components (at 350 m depth) aligned with their respective principal axis directions.

There is weak evidence of Ekman pumping in the form of coherence between wind stress curl and temperature at the ~ 350 m level, and essentially the same

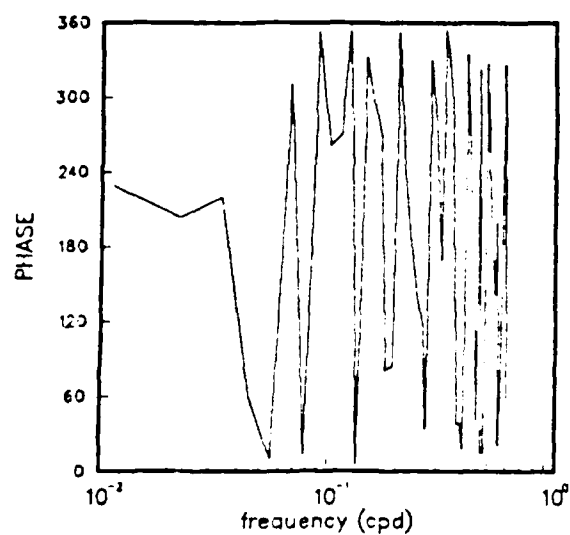
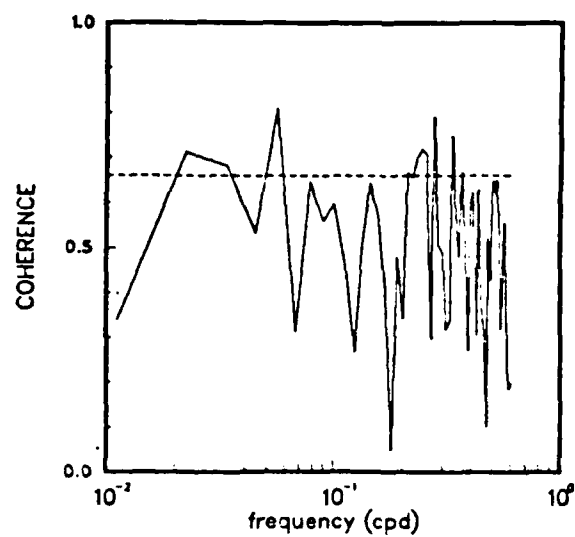


Figure 4.5 Coherence and phase between wind stress curl and current component 30° east of north at M1-375.

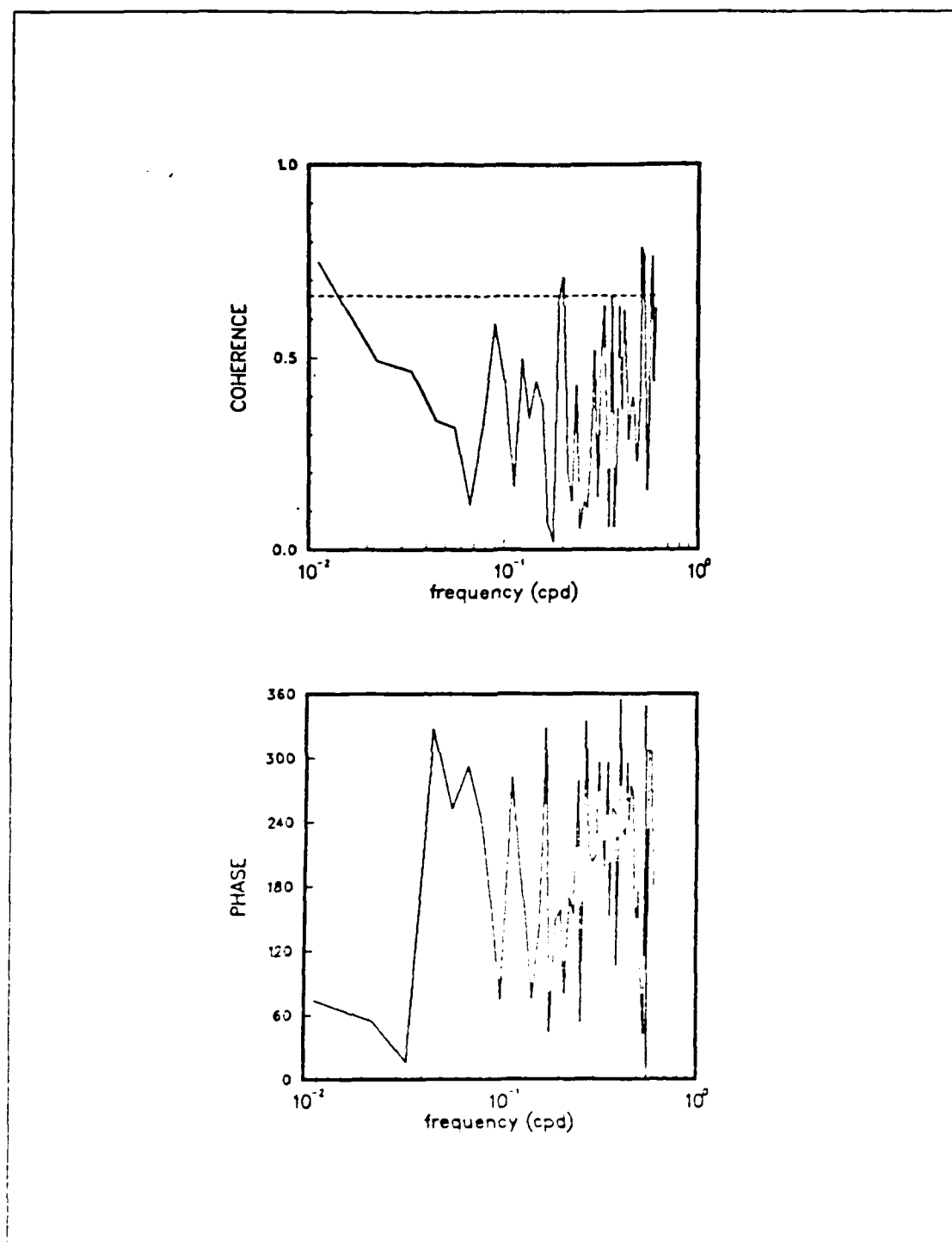


Figure 4.6 As in Figure 4.5, but for M2-340 and 120° east of north.

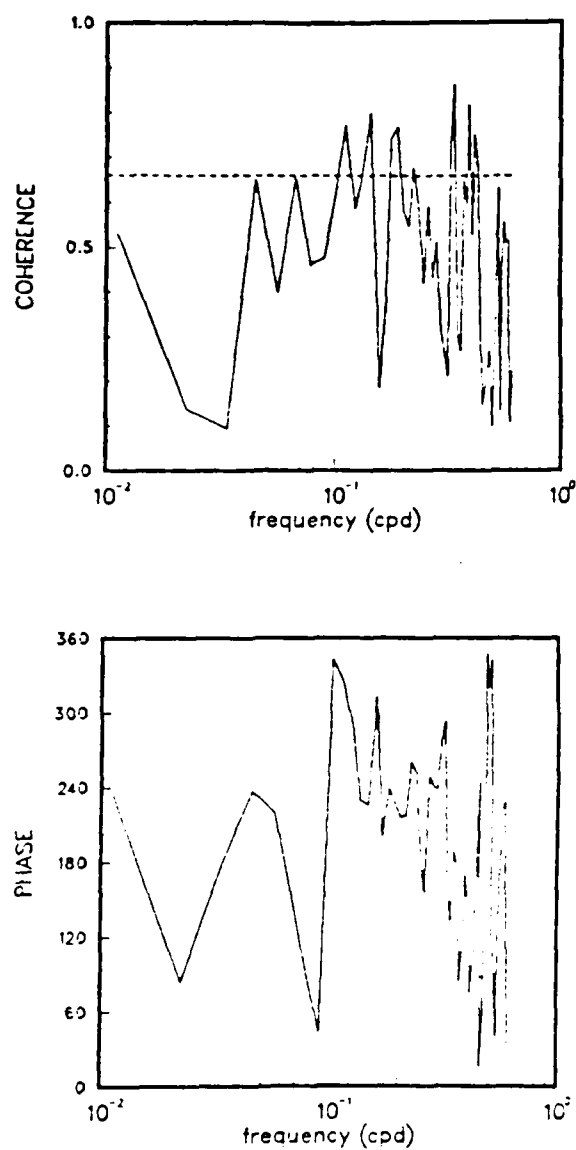


Figure 4.7 Coherence and phase between meridional wind stress and meridional component of barotropic mode, M1.

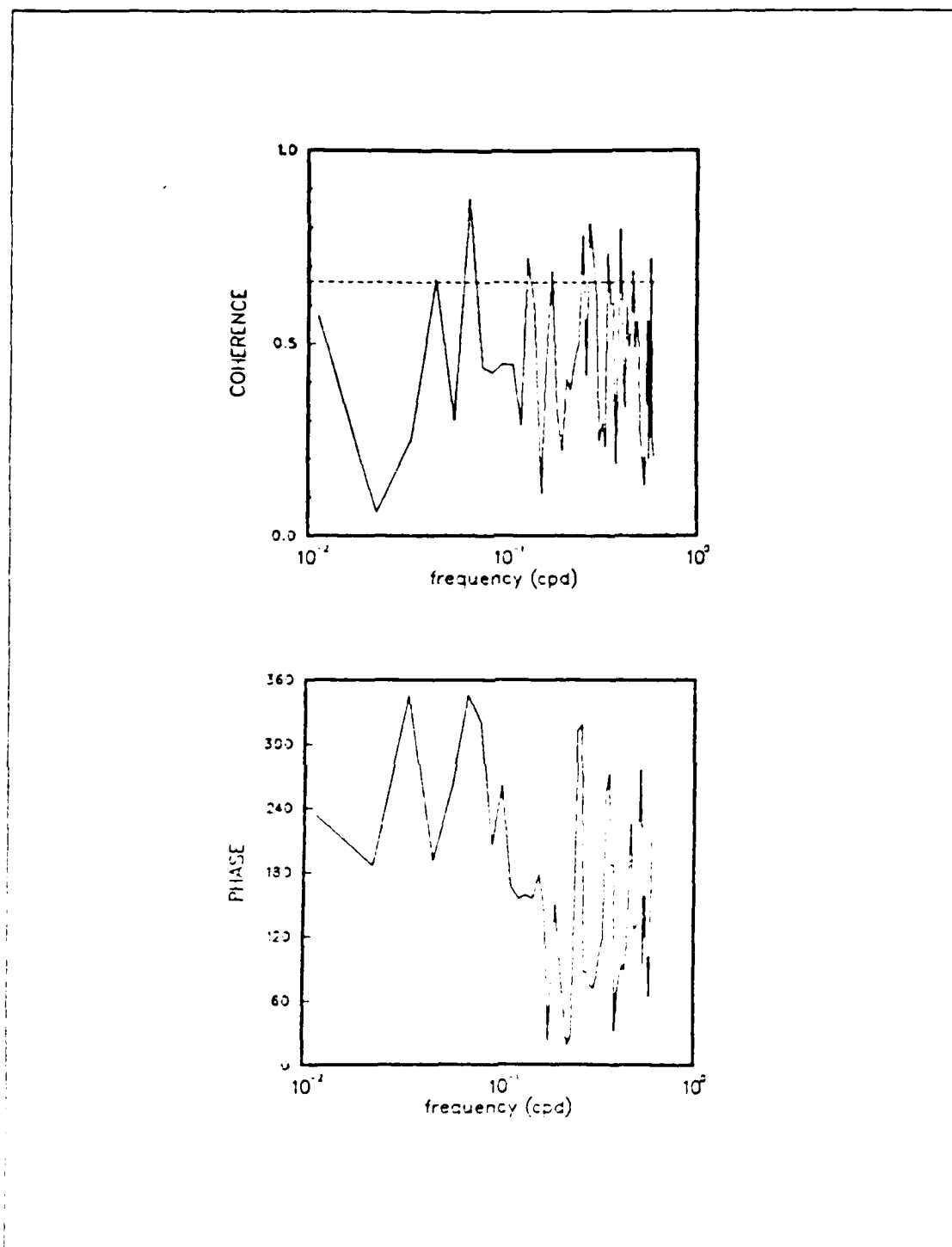


Figure 4.8 As in Figure 4.7, but with the first baroclinic mode, M1.

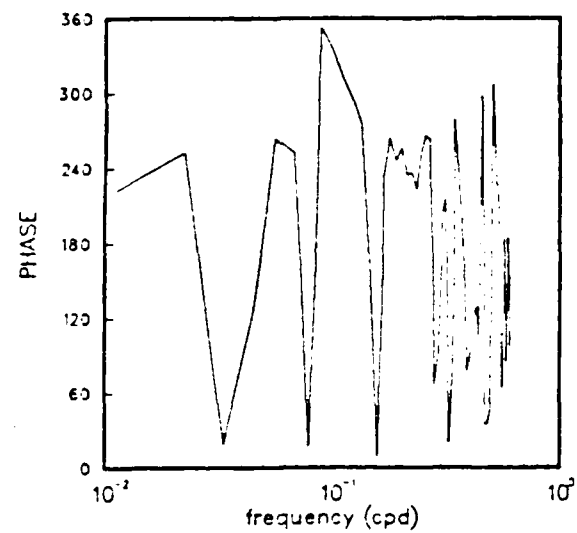
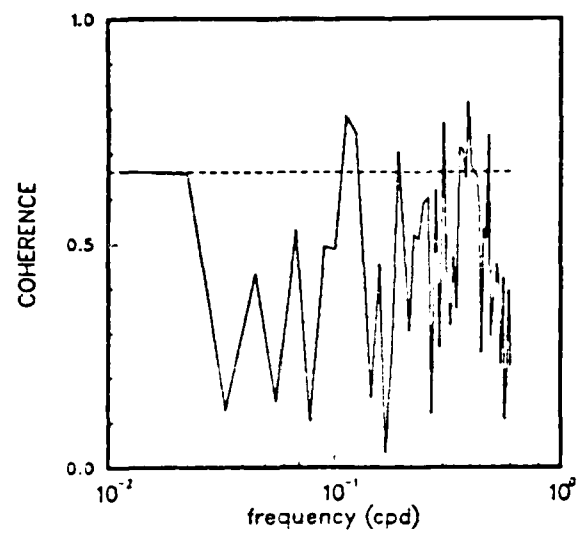


Figure 4.9 As in Figure 4.7, but with the barotropic mode, M2.

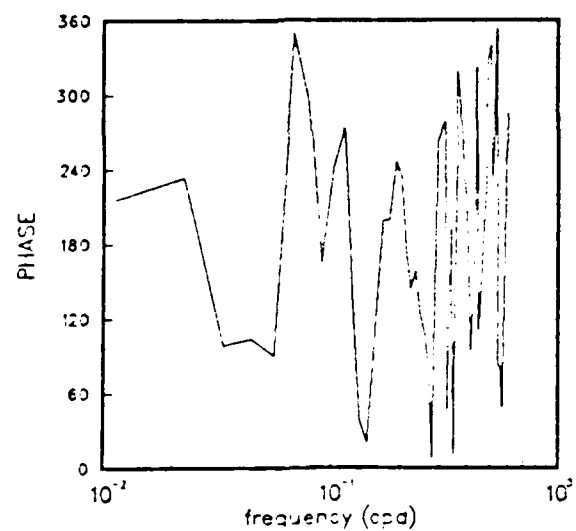
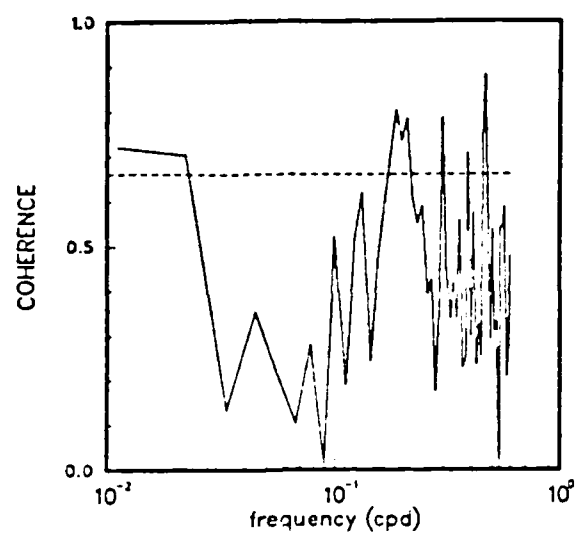


Figure 4.10 As in Figure 4.7, but with the first baroclinic mode, M2.

between $\partial T/\partial t$ and $\nabla \times \tau$. Neither wind stress curl nor temperature is coherent with horizontal divergence computed at the 350 m level, but alongshore divergence between M1 and M2 is coherent with temperature at M3-350 (farther offshore) at low frequency. Horizontal advection masks the evidence for Ekman pumping. To see if masking of the current response to wind stress curl may be due to coastal effects, the results are compared to those for mooring CMMW10, one of the LLWOD moorings analyzed by Stabeno and Smith (1986), Figure 3.1. CMMW10, with five current meters, was deployed approximately 200 km northwest of the OPTOMA mooring locations for ~ 10 months in 1982-83. There is very little coherence between $\nabla \times \tau$ and either temperature or $\partial T/\partial t$ at mooring CMMW10, however, CMMW10 was located very close to the $\nabla \times \tau$ longitude off the northern California coast (Nelson, 1977). Hence, the much less energetic $\nabla \times \tau$ forcing over CMMW10 may account for the lack of coherence with temperature and $\partial T/\partial t$.

At moorings M1 and M2, the barotropic and first baroclinic dynamical mode components are coherent with corresponding wind stress components, but at different periods for the two modes. The v-component of the barotropic mode at CMMW10 is coherent with τ_y at periods of 8 and 16 days, Figure 4.11. The v-component of the first baroclinic mode at CMMW10 is coherent with τ_y at the same periods, Figure 4.12, in contrast to M1 and M2 where the barotropic and baroclinic responses were at different periods. This could be a result of simpler dynamics in the CMMW10 regime (simpler bottom topography, farther from the coast) than in the OPTOMA domain. For example, the ratio of long-term integrated energy in the barotropic and first baroclinic modes is 0.64 for M2 and 1.84 for CMMW10. However, M2 and CMMW10 were deployed in different years, and this alone could account for the observed differences.

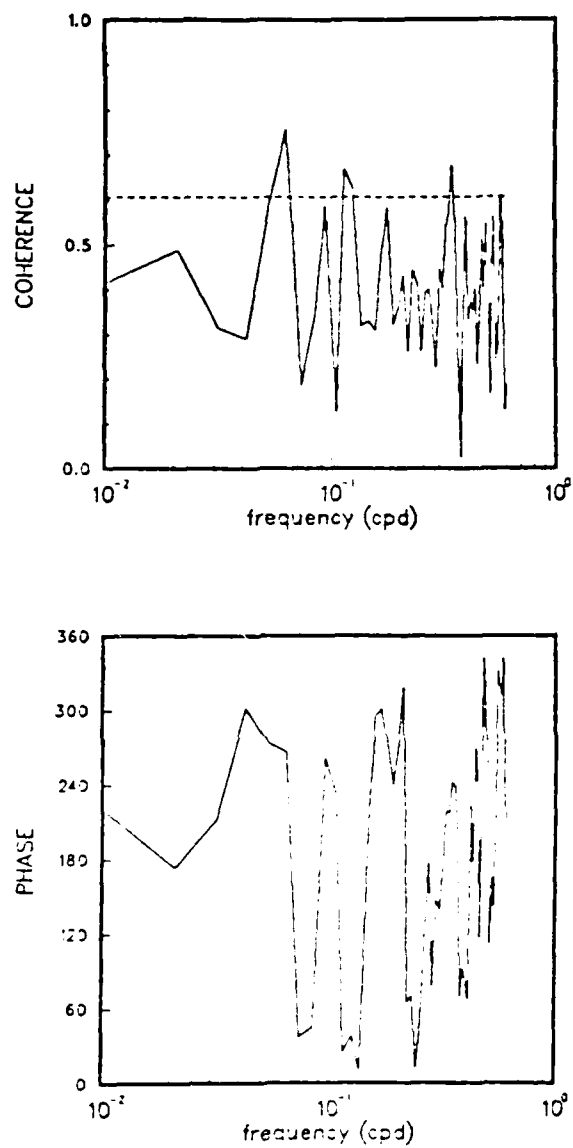


Figure 4.11 As in Figure 4.7, but with the barotropic mode, CMMW10.

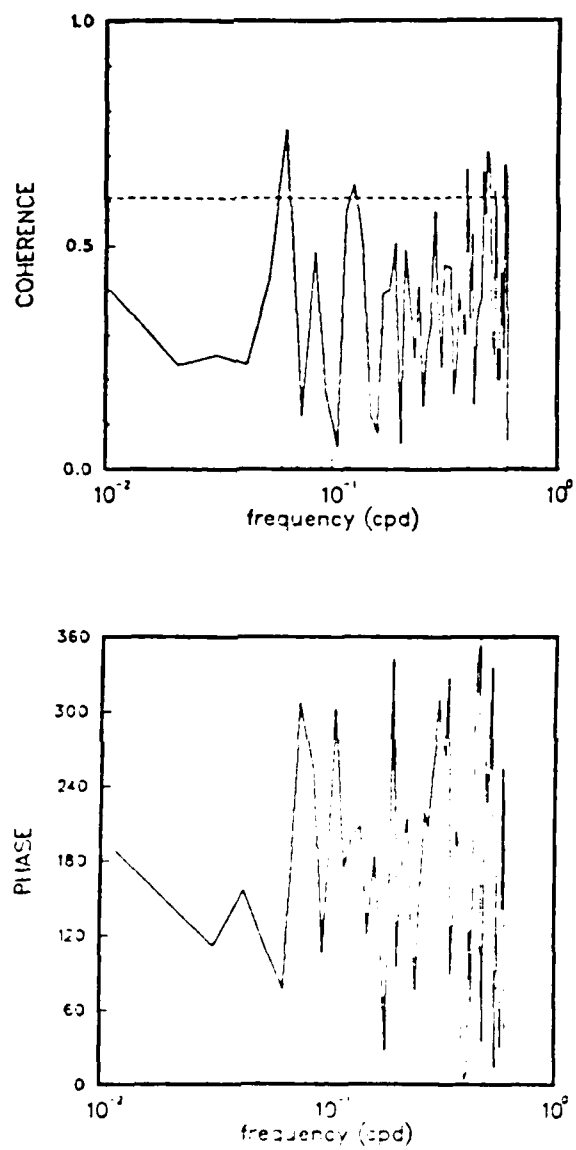


Figure 4.12 As in Figure 4.7, but with the first baroclinic mode, CMMW10.

V. SUMMARY AND CONCLUSIONS

A. SUMMARY

This study has examined the oceanic response to wind forcing by analyzing moored current meter records with FNOC surface wind analyses. There is coherence, to one degree or another, between wind forcing and ocean current variables in all three frequency ranges defined by Willebrand *et. al.*, (1980), and the results are summarized by these ranges.

1. *Locally Forced Response (1-10 day period)*

There are many coherent peaks in the cross-spectra of wind stress and ocean currents. These peaks are concentrated at periods of 3-to-9 days and are very robust, being in the component-wise planar cross-spectra of wind stress and current for every mooring and level. The large grid spacing of the FNOC wind analyses (~ 330 km at the latitude of this study) is probably too large to resolve all of the wind features that are forcing the oceanic response in this frequency band, which may account for some of the imperfection in wind stress/current coherence in this band. The importance of horizontal advective processes in the study area may also account for some of the imperfections in wind stress/current coherence in this band, although, in this study, the evidence of the advective processes is at much longer periods.

2. *Planetary Wave Response (10-30 day periods)*

Very little coherence between atmospheric and oceanic variables is found in this range, except for M1-3250. The autospectrum of M1-3250 has a large peak centered at a period of ~ 13 days, which may represent the free, bottom-trapped topographic waves observed in the model results of Willebrand *et. al.* (1980). These bottom-trapped topographic waves were generated in their model by vertical motion produced as the wind-induced flow interacted with topography. The large peak in the M1-3250 spectrum in this frequency range is possibly evidence of this process.

Limited evidence of Ekman pumping is also found in this frequency range. Temperature changes at 350 m depth are coherent with wind stress at periods of 14, 18, and 28 days, as well as at long periods (> 67 days).

3. Sverdrup Balance Response (> 30 day periods)

Evidence of the Sverdrup balance is found at M1, where $U \bullet \nabla(f/H)$ is coherent with wind stress curl for periods of 18 and 28-50 days. The M1 results agree with those of Niiler and Koblinsky (1985), who found evidence of the Sverdrup balance at 10-100 day periods (albeit much farther offshore). The coherence between wind stress curl and $U \bullet \nabla(f/H)$ for other periods at M1 and for all periods at M2 and M3 is most likely destroyed by the horizontal advective processes that appear to dominate variability in the upper levels of the water column in the study area.

4. Effects of Bottom Topography

The degree of coherence between wind forcing and current variables varies markedly horizontally and vertically. Model results suggest that bottom topography may account for much of this inhomogeneity. The results of numerical experiments with smoothed bottom topography, homogeneous ocean, and stochastic wind forcing show considerable horizontal variation in the current spectrum over short distances (Willebrand *et al.*, 1980). Similar experiments with a stratified ocean demonstrated that topography leads to mode coupling and energy exchange between modes (Muller and Frankignoul, 1981). It is likely that the fairly complicated bottom topography in the vicinity of the OPTOMA moorings significantly alters the flow and partially destroys any coherence with wind forcing.

5. Coastal Effects

The proximity of the coast to the OPTOMA mooring locations is a major complicating factor that may partially destroy wind-current coherence. Satellite infrared images of the Oregon and northern California coast contain many cool filaments and meandering jets extending offshore through the OPTOMA domain (Ikeda and Emery, 1984). These cool filaments and meandering jets have accompanying current filaments below the surface which can also be seen in hydrographic data (Mooers and Robinson, 1984). Alongshore divergence between M1 and M2 at 350 m depth is coherent with temperature changes at M3 (100 km farther offshore), consistent with offshore advection by CCS current filaments. These results indicate that the CCS current filaments extend at least as deep as 350 m.

In summary, the oceanic response to wind forcing in the OPTOMA domain is very complex. The results of this study are not inconsistent with earlier model and observational studies. The close proximity of the continental slope (about one Rossby radius away) and the strong advective processes that appear to dominate upper level

variability in the study area make it definitely unlike a mid-ocean regime, but it is too far removed from the coast to be affected by coastal jets as observed by Kundu and Allen (1976), coastally trapped waves, or other strictly coastal processes. Hence, the OPTOMA domain is neither mid-ocean nor coastal in nature.

Overall, the issues raised here are important for the development of ocean circulation models, observing systems, and ocean prediction systems for eastern boundary current regimes. To date, the OPTOMA program has been able to ignore atmospheric forcing and to proceed without current meter data in ocean prediction studies. This has been at the expense of using much XBT and CTD data. The present results provide the hope that an atmospheric forcing prescription could possibly be economically traded-off, with the use of appropriate models, against mass field data in future ocean prediction studies. Presumably, there would also be an important role, yet to be established, for current meter data in such studies.

B. RECOMMENDATIONS

This study is a first step in describing the oceanic response to wind forcing in an eastern boundary current regime like the OPTOMA domain. Future studies should examine the OPTOMA current data for coherence with distant winds, as found in model studies by Carton (1984) and in observational studies of wind stress and sea level response very close to the coast by Halliwell and Allen (1984). Analysis of the OPTOMA current records should also be undertaken with wind forcing information from other available sources (such as meteorological buoy wind data and the National Meteorological Center's LFM and NGM wind analyses) that may resolve wind features of smaller scale than the scales resolvable by the FNOC grid spacing. The results of this study show that there is a considerable amount of mesoscale ocean variability in the OPTOMA domain that is of too small a scale to be resolvable by the 100 km spacing used for moorings M1, M2, and M3. Clearly, more (and more closely spaced) current meter moorings will be required to describe fully all of the horizontal variability in this region. Current records closer to the surface will be required to adequately sample the effects from the coastal transition zone.

APPENDIX A

PROCESSING AND ANALYSIS OF FNOC WIND DATA

FNOC surface wind analyses, on a 63×63 Northern Hemisphere polar stereographic grid, are generated at 6 hour intervals using NOGAPS (Navy Operational Global Atmospheric Prediction System) forecast fields as first-guess analysis fields, to which new data are added using a form of the successive corrections interpolation technique (Rosmond, 1981). These analyses are archived on a 6 hour cycle (00Z, 06Z, 12Z, 18Z) and are used to re-initialize the NOGAPS global atmospheric forecast model.

The time gaps in the FNOC analyses were identified and the duplicate records deleted on a first editing pass. Data points that were clearly spurious in magnitude (differed from the mean by more than 3σ , where σ is the standard deviation) were also omitted. Data gaps were found to be short (of 24 hours or less), and they were filled by simple linear interpolation. The use of a higher order polynomial or statistical interpolation would probably be required to fill larger gaps satisfactorily.

An iterative technique which assumed a neutral flux profile was used to adjust the FNOC values, which are at a height of 19.5 m, to 10 m, at which the wind stress was computed. No change was made to wind direction. The computation used the neutral flux drag coefficient of Large and Pond (1981), and the iterative scheme is outlined below. Given:

u_{19} : u wind component from FNOC data

v_{19} : v wind component from FNOC data

κ : Von Karman's constant

ϵ : convergence criteria for adjustment factor

C_d : drag coefficient

u_* : friction velocity

g : acceleration due to gravity

Let:

$$|V|_0 = (u_{19}^2 + v_{19}^2)^{1/2}$$

$$\kappa = 0.4$$

$$\varepsilon = 0.1$$

$$g = 9.8 \text{ m/s}$$

Begin the iteration:

$$\begin{aligned} (10^3 C_d)_k &= 1.14, \quad |V|_k < 10 \text{ m/s} \\ &= 0.49 + 0.065|V|_k, \quad |V|_k \geq 10 \text{ m/s} \end{aligned}$$

$$(u_*)_k = (u_*)_{k-1} (C_d)^{1/2}$$

$$\eta = \frac{[\ln(10.0g/u_*^2)/\kappa] - 10.6}{[\ln(19.5g/u_*^2)/\kappa] - 10.6}$$

$$|V|_k = |V|_0 \eta$$

The iteration continues until $||V|_k - |V|_{k-1}| < \varepsilon$. Then, the adjustment factor, μ , is given by:

$$\mu = |V|_k / |V|_0$$

Finally,

$$u_{10} = \mu u_{19}$$

$$v_{10} = \mu v_{19}$$

The FNOC polar stereographic projection is true at 60N. Using indices 0-62, the pole is at (31,31). The 80W meridian is aligned with $i=31$ on the grid. The grid spacing, Δx , is 381 km at 60N and varies with latitude:

$$\Delta x = (381)[(1 + \sin \varphi)/1.866],$$

where φ is the latitude. Given the (i,j) coordinates of a polar stereographic grid point, latitude and longitude (λ) of the point may then be computed by (e.g., Haltiner and Williams, 1980):

$$\lambda = 10^\circ + \tan^{-1}(y_j/x_i)$$

$$\varphi = \sin^{-1}[(z^2 - y_j^2)/(z^2 + y_j^2)], \text{ where}$$

$$z = a[1 + (\sin 60^\circ)]\sin \theta,$$

$$\theta = \lambda - 10^\circ,$$

$$a = 6371 \text{ km (radius of a sphere with same volume as earth),}$$

$$x_i = (i-31)381, \text{ and}$$

$$y_j = (j-31)381.$$

The u and v wind components (u_{ps}, v_{ps}) obtained from FNOC data are referenced to the polar stereographic grid coordinate frame. The u and v components in geographic (i.e., E-W/N-S) coordinates (u_m, v_m) are given by:

$$u_m = -u_{ps}(\sin \gamma) + v_{ps}(\cos \gamma)$$

$$v_m = -u_{ps}(\cos \gamma) - v_{ps}(\sin \gamma)$$

where $\gamma = \tan^{-1}(y_j/x_i)$. Wind speed and direction information that are relative to true north are also available from FNOC.

The processing outlined in this appendix was applied to the FNOC surface analysis data to generate a wind time series at 10 m for each grid point of interest. The wind stress may now be computed:

$$\tau_x = \rho_a C_d U u_{10}, \text{ and}$$

$$\tau_y = \rho_a C_d U v_{10}, \text{ where}$$

$$\rho_a = 1.225 \times 10^{-3} \text{ gm cm}^{-3} \text{ (air density), and}$$

$$|U| = (u_{10}^2 + v_{10}^2)^{1/2},$$

and u_{10} and v_{10} are in either geographic or polar stereographic coordinates.

Haney *et. al.* (1981) gives the formula for the wind stress curl:

$$\nabla \times \tau = m^2 [\partial_x (\tau_y / m) - \partial_y (\tau_x / m)],$$

where m is the map factor (see Haltiner and Williams, 1980):

$$m(\phi) = (1 + \sin 60^\circ) (1 + \sin \phi),$$

and τ_x and τ_y are in the polar stereographic reference frame. Wind stress time series from four (in a square configuration) grid points or three (in a triangle) may be used to

compute finite difference approximations to the derivatives in the equation for $\nabla \times \tau$ above. The geographic center of the current meter array used in this study is positioned with respect to the FNOC grid such that use of the square scheme to compute wind stress curl requires that a grid point over land be used in the computation. Use of the triangular scheme allows exclusion of the grid point over land from the computation.

Wind stress curl time series using both of these schemes were analyzed to see if the larger truncation error associated with the triangular scheme was significant. The time series derived from the square (F-G-J-K, Figure 2.1) and triangular (F-J-K, Figure 2.1) schemes look virtually identical, Figure A.1. The autospectra of the $\nabla \times \tau$ time series derived from the square and triangular schemes are very similar with only minor differences detectable, Figure A.2. The time series of $\nabla \times \tau$ from these schemes are coherent for all periods less than 90 days, Figure A.3. Hence, the effect of additional truncation error of the triangular scheme is not readily apparent.

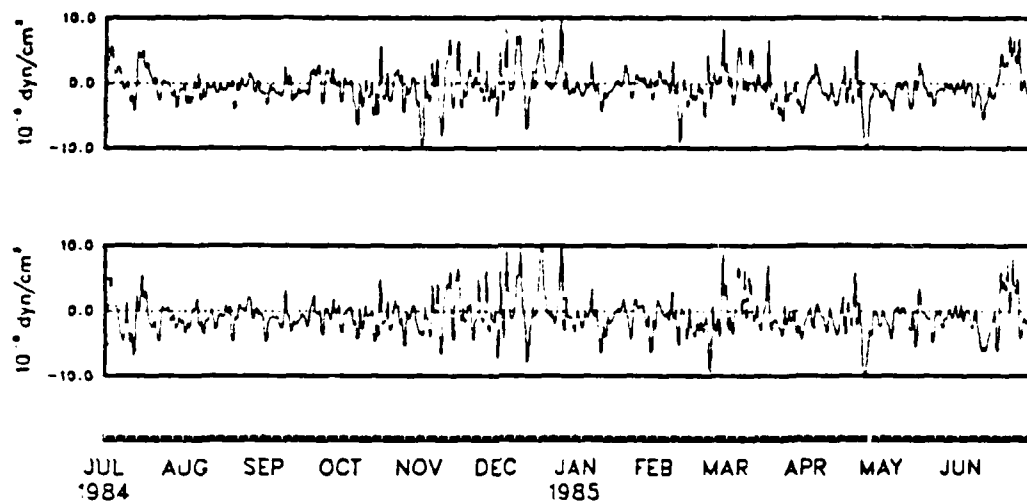


Figure A.1 Time series of wind stress curl derived from square (top) and triangular (bottom) schemes.

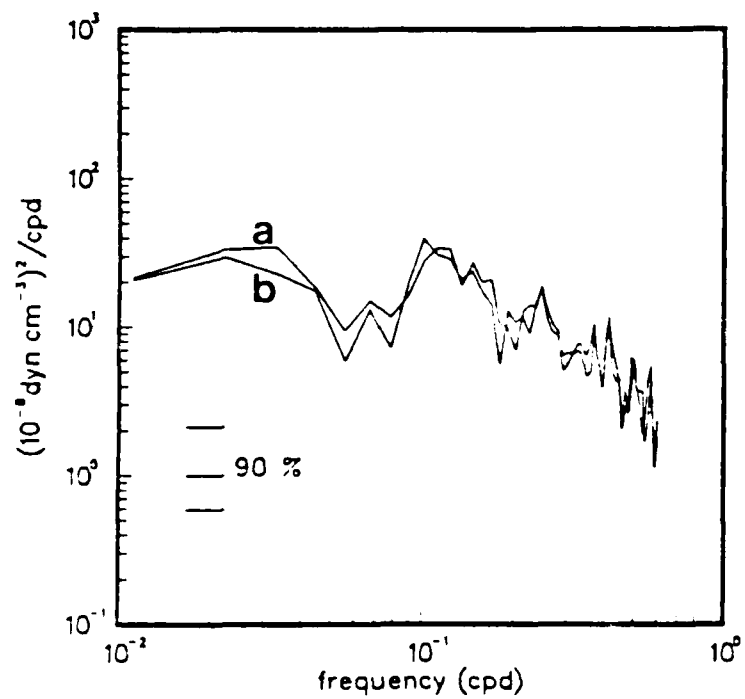


Figure A.2 Autospectra of wind stress curl computed with square (a) and triangular (b) schemes.

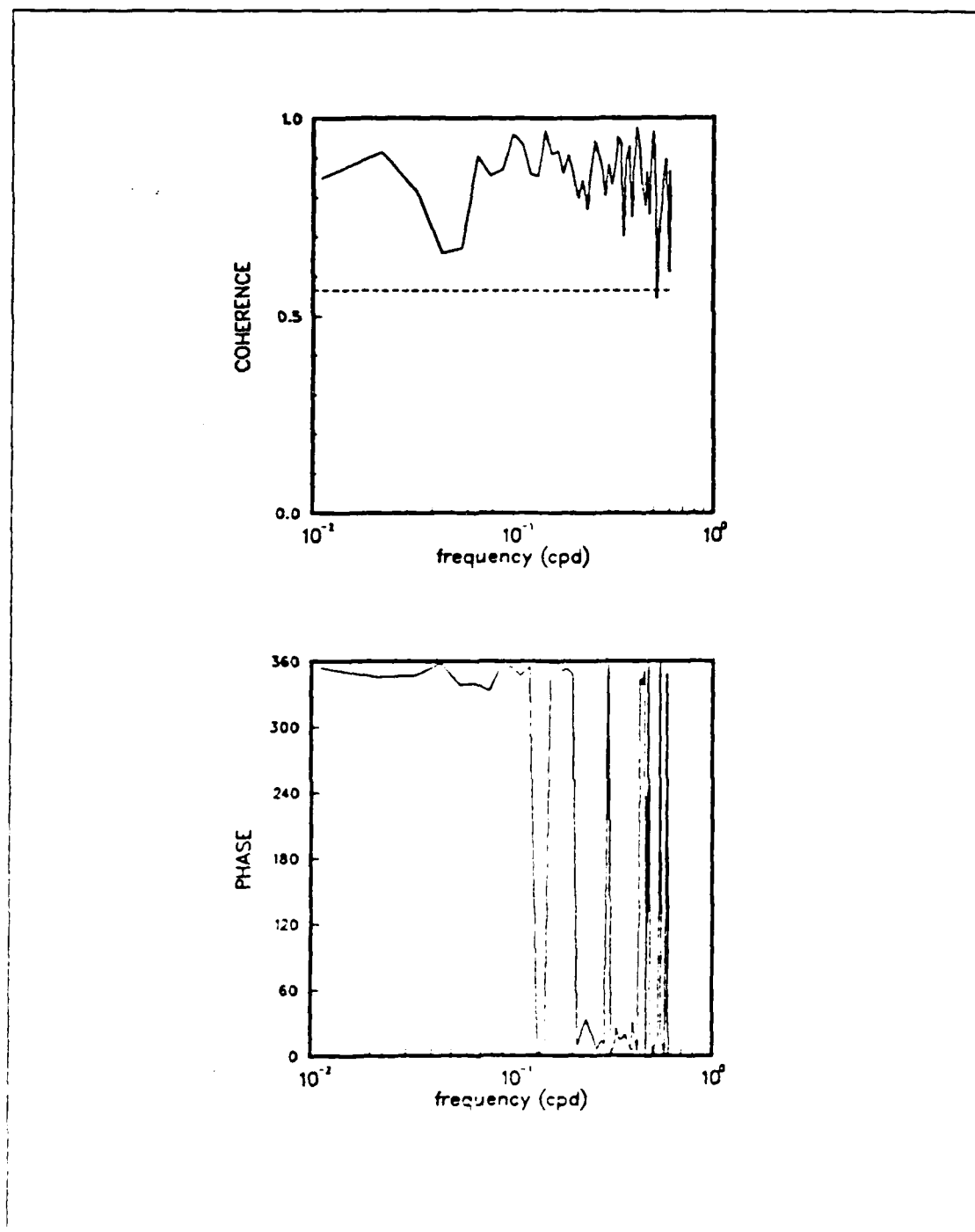


Figure A.3 Coherence and phase between square and triangular schemes.

LIST OF REFERENCES

- Carton, J.A., 1984: Coastal circulation caused by an isolated storm. *J. Phys. Oceanogr.*, **14**, 114-124.
- Frankignoul, C., and P. Muller, 1979: Quasi-geostrophic response of an infinite β -plane ocean to stochastic forcing by the atmosphere. *J. Phys. Oceanogr.*, **9**, 104-127.
- Gill, A.E., 1982: *Atmosphere-Ocean Dynamics*, Academic Press, Inc., 662 pp.
- Gonella, J., 1972: A rotary-component method for analysing meteorological and oceanographic vector time series. *Deep Sea Res.*, **19**, 833-846.
- Halliwel, G.R. Jr., and J.S. Allen, 1984: Large-scale sea level response to atmospheric forcing along the west coast of North America, Summer 1973. *J. Phys. Oceanogr.*, **14**, 864-886.
- , and ———, 1986: The large-scale coastal wind field along the west coast of North America, 1981-1982. *J. Geophys. Res.*, in press.
- Haltiner, G.J., and R.T. Williams, 1980: *Numerical Prediction and Dynamic Meteorology*, 2nd edition, John Wiley and Sons Inc., 477 pp.
- Haney, R.L., M.S. Risch and G.C. Heise, 1981: Wind forcing due to synoptic storm activity over the North Pacific Ocean. *Atmos.-Ocean*, **19**, 128-147.
- Heath, G.R., D.K. Rea, G. Ness, R.D. Pillsbury, T.M. Beasley and C. Lopez, 1984: Oceanographic studies supporting the assessment of deep-sea disposal of defueled decommissioned nuclear submarines. *Environ. Geol. Water Sci.*, **6**(4), 189-199.
- Hickey, B.M., 1979: The California Current System - hypothesis and facts. *Prog. in Oceanogr.*, **8**, 191-279.
- Ikeda, M., and W.J. Emery, 1984: Satellite observations and modeling of meanders in the California Current System off Oregon and Northern California. *J. Phys. Oceanogr.*, **14**, 1434-1450.
- Kundu, P.K., and J.S. Allen, 1976: Some three-dimensional characteristics of low-frequency current fluctuations near the Oregon coast. *J. Phys. Oceanogr.*, **6**, 181-199.
- Large, W.G., and S. Pond, 1981: Open ocean momentum flux measurements in moderate to strong winds. *J. Phys. Oceanogr.*, **11**, 324-336.
- Mooers, C.N.K., 1973: A technique for the cross spectrum analysis of pairs of complex-valued time series, with emphasis on properties of polarized components and rotational invariants. *Deep Sea Res.*, **20**, 1129-1141.
- , and A.R. Robinson, 1984: Turbulent jets and eddies in the California Current and inferred cross-shore transports. *Science*, **223**, 51-53.
- Muller, P., and C. Frankignoul, 1981: Direct atmospheric forcing of geostrophic eddies. *J. Phys. Oceanogr.*, **11**, 287-308.
- Nelson, C.S., 1977: Wind stress and wind stress curl over the California Current. *NOAA Tech. Rep. NMFS SSRF-714*, U.S. Dep. Commer., 57 pp.
- Niiler, P.P., and C.J. Kohlinsky, 1985: A local time-dependent Sverdrup balance in the eastern North Pacific Ocean. *Science*, **229**, 754-756.
- Noble, M., R.C. Beardsley, J.V. Gardner and R.L. Smith, 1986: Observations of subtidal currents over the northern California continental slope and adjacent basin: some evidence for local wind forcing. Submitted to: *J. Geophys. Res.*

- Philander, S.G.H., and J.-H. Yoon, 1982: Eastern boundary currents and coastal upwelling. *J. Phys. Oceanogr.*, **12**, 862-879.
- Richman, J.G., C. Wunsch and N.G. Hogg, 1977: Space and time scales of mesoscale motion in the western North Atlantic. *Rev. Geophys. Space Phys.*, **15**, 385-420.
- Rienecker, M.M., C.N.K. Mooers, R.L. Smith, P.J. Stabeno and S.J. Summers, 1986: Low-frequency variability in the California Current System off northern California. Manuscript in preparation.
- Robinson, A.R., J.A. Carton, N. Pinardi and C.N.K. Mooers, 1986: Dynamical forecasting and dynamical interpolation: an experiment in the California Current. *J. Phys. Oceanogr.*, in press.
- Rosmond, T.E., 1981: NOGAPS: Navy Operational Global Atmospheric Prediction System. *Fifth Conf. Num. Wea. Pred.*, Amer. Met. Soc., 74-79.
- Saunders, P.M., 1976: On the uncertainty of wind stress curl computations. *J. Mar. Res.*, **34**, 155-160.
- Smith, R.L., G. Pittock, J. Fleischbein and R. Still, 1986: Current measurements from moorings off Northern California: September 1984 - July 1985. Oregon State University, College of Oceanography, Ref. 86-6, 211 pp.
- Stabeno, P.J., and R.L. Smith, 1986: Deep sea currents off northern California. Submitted to: *J. Geophys. Res.*
- Thompson, R.O.R.Y., 1983: Low-pass filters to suppress inertial and tidal frequencies. *J. Phys. Oceanogr.*, **13**, 1077-1083.
- Willebrand, J., S.G.H. Philander and R.C. Pacanowski, 1980: The oceanic response to large-scale atmospheric disturbances. *J. Phys. Oceanogr.*, **10**, 411-429.

INITIAL DISTRIBUTION LIST

| | No. Copies |
|--|------------|
| 1. Defense Technical Information Center Cameron Station Alexandria, VA 22304-6145 | 2 |
| 2. Library, Code 0142 Naval Postgraduate School Monterey, CA 93943-5002 | 2 |
| 3. Chairman (Code 68Mr) Department of Oceanography Naval Postgraduate School Monterey, CA 93943 | 2 |
| 4. Chairman (Code 63Rd) Department of Meteorology Naval Postgraduate School Monterey, CA 93943 | 1 |
| 5. Dr. M.M. Rienecker (Code 68Rw) Department of Oceanography Naval Postgraduate School Monterey, CA 93943 | 2 |
| 6. Professor R.L. Smith College of Oceanography Oregon State University Corvallis, OR 97331 | 1 |
| 7. Professor R.L. Haney (Code 63Hy) Department of Meteorology Naval Postgraduate School Monterey, CA 93943 | 1 |
| 8. Professor A.R. Robinson Division of Applied Sciences Pierce Hall Room 100D Harvard University Cambridge, MA 02138 | 1 |
| 9. LCDR Steven. J. Summers, USN 1408 E. Gorman Rd. Adrian, MI 49221 | 2 |
| 10. Director Naval Oceanography Division Naval Observatory 34th and Massachusetts Avenue NW Washington, DC 20390 | 1 |
| 11. Commander Naval Oceanography Command NSTL Station Bay St. Louis, MS 39522 | 1 |
| 12. Commanding Officer Naval Oceanographic Office NSTL Station Bay St. Louis, MS 39522 | 1 |

- | | | |
|-----|---|---|
| 13. | Commanding Officer Fleet Numerical Oceanography Center Monterey, CA 93943 | 1 |
| 14. | Commanding Officer Naval Ocean Research and Development Activity NSTL Station Bay St. Louis, MS 39522 | 1 |
| 15. | Commanding Officer Naval Environmental Prediction Research Facility Monterey, CA 93943 | 1 |
| 16. | Chairman, Oceanography Department U.S. Naval Academy Annapolis, MD 21402 | 1 |
| 17. | Chief of Naval Research 800 N. Quincy Street Arlington, VA 22217 | 1 |
| 18. | Office of Naval Research (Code 420) Naval Ocean Research and Development Activity 800 N. Quincy Street Arlington, VA 22217 | 1 |
| 19. | Scientific Liason Office Office of Naval Research Scripps Institution of Oceanography La Jolla, CA 92037 | 1 |
| 20. | Commander Oceanographic Systems Pacific Box 1390 Pearl Harbor, HI 96860 | 1 |
| 21. | Commanding Officer Naval Eastern Oceanography Center Naval Air Station Norfolk, VA 23511 | 1 |
| 22. | Commanding Officer Naval Western Oceanography Center Box 113 Pearl Harbor, HI 96860 | 1 |
| 23. | Commanding Officer Naval Oceanography Command Center, Rota Box 31 FPO San Francisco, CA 09540 | 1 |
| 24. | Commanding Officer Naval Oceanography Command Center, Guam Box 12 FPO San Francisco, CA 96630 | 1 |

END

2-87

DTIC